NAVAL POSTGRADUATE SCHOOL

MONTEREY, CALIFORNIA

THESIS

CHARACTERIZATION OF INTERNAL WAVES AND TIDES OVER A CALDERA IN THE NEW ENGLAND SEAMOUNT CHAIN AND THEIR IMPACT ON SHORT-TERM ACOUSTIC PATH AVAILABILITY

by

Braydon M. Hammond

June 2023

Thesis Advisor:	John A. Colosi
Co-Advisor:	Kay L. Gemba
Second Reader:	Derek Olson

THIS PAGE INTENTIONALLY LEFT BLANK

REPORT DOCUMENTATION PAGE	*Form Approved OMB No. 0704-0188*

1. AGENCY USE ONLY *(Leave blank)*	**2. REPORT DATE** June 2023	**3. REPORT TYPE AND DATES COVERED** Master's thesis

4. TITLE AND SUBTITLE
CHARACTERIZATION OF INTERNAL WAVES AND TIDES OVER A CALDERA IN THE NEW ENGLAND SEAMOUNT CHAIN AND THEIR IMPACT ON SHORT-TERM ACOUSTIC PATH AVAILABILITY

5. FUNDING NUMBERS

6. AUTHOR(S) Braydon M. Hammond

7. PERFORMING ORGANIZATION NAME(S) AND ADDRESS(ES)
Naval Postgraduate School
Monterey, CA 93943-5000

8. PERFORMING ORGANIZATION REPORT NUMBER

9. SPONSORING / MONITORING AGENCY NAME(S) AND ADDRESS(ES)
N/A

10. SPONSORING / MONITORING AGENCY REPORT NUMBER

11. SUPPLEMENTARY NOTES The views expressed in this thesis are those of the author and do not reflect the official policy or position of the Department of Defense or the U.S. Government.

12a. DISTRIBUTION / AVAILABILITY STATEMENT
Approved for public release. Distribution is unlimited.

12b. DISTRIBUTION CODE
A

13. ABSTRACT (maximum 200 words)

In pursuit of understanding the relationship between oceanography and acoustics, this thesis characterizes sound-speed fluctuations from moored Conductivity, Temperature, and Depth (CTD) observations in the New England Seamount Chain (NESC) and estimates their impact on acoustic path availability using normal mode and ray theory. A single vertical mooring with oceanographic instruments was deployed in the summer of 2022 over a 3000 m tall caldera in the NESC to quantify the vertical and temporal scales of the fluctuating water column in the Sargasso and Slope seas. Dominant oceanographic processes in the NESC include the Gulf Stream current, eddies, and internal waves (IWs). Isotherm displacements are analyzed with visual and spectral techniques to quantify impacts from these phenomena. Isotherm displacements are greater in the Slope Sea than the Sargasso Sea, which is evident from filtered high pass isotherms and IW spectral variances. Isotherm spectra indicate the presence of a semidiurnal internal tide, tidal harmonics, and random high-frequency IWs above the caldera. The frequency-dependent normal mode structure of a subsurface duct in the Sargasso Sea is strongly impacted by eddies and IWs. Acoustic path availability near the Atlantis II seamount is investigated using ray theory, which identifies exploitable acoustic paths with minimal boundary interactions. A ray simulation with IW sound speed perturbations demonstrates an increase in exploitable acoustic paths.

14. SUBJECT TERMS
acoustic oceanography, ocean acoustics, ray theory, internal waves, internal tides, isotherm displacement, tactical oceanography, bathymetry, seamounts, vertical mooring

15. NUMBER OF PAGES
81

16. PRICE CODE

17. SECURITY CLASSIFICATION OF REPORT	**18. SECURITY CLASSIFICATION OF THIS PAGE**	**19. SECURITY CLASSIFICATION OF ABSTRACT**	**20. LIMITATION OF ABSTRACT**
Unclassified	Unclassified	Unclassified	UU

NSN 7540-01-280-5500

Standard Form 298 (Rev. 2-89)
Prescribed by ANSI Std. 239-18

THIS PAGE INTENTIONALLY LEFT BLANK

Approved for public release. Distribution is unlimited.

CHARACTERIZATION OF INTERNAL WAVES AND TIDES OVER A CALDERA IN THE NEW ENGLAND SEAMOUNT CHAIN AND THEIR IMPACT ON SHORT-TERM ACOUSTIC PATH AVAILABILITY

Braydon M. Hammond
Ensign, United States Navy
BS, United States Naval Academy, 2022

Submitted in partial fulfillment of the
requirements for the degree of

MASTER OF SCIENCE IN PHYSICAL OCEANOGRAPHY

from the

NAVAL POSTGRADUATE SCHOOL
June 2023

Approved by: John A. Colosi
Advisor

Kay L. Gemba
Co-Advisor

Derek Olson
Second Reader

Peter C. Chu
Chair, Department of Oceanography

THIS PAGE INTENTIONALLY LEFT BLANK

ABSTRACT

In pursuit of understanding the relationship between oceanography and acoustics, this thesis characterizes sound-speed fluctuations from moored Conductivity, Temperature, and Depth (CTD) observations in the New England Seamount Chain (NESC) and estimates their impact on acoustic path availability using normal mode and ray theory. A single vertical mooring with oceanographic instruments was deployed in the summer of 2022 over a 3000 m tall caldera in the NESC to quantify the vertical and temporal scales of the fluctuating water column in the Sargasso and Slope seas. Dominant oceanographic processes in the NESC include the Gulf Stream current, eddies, and internal waves (IWs). Isotherm displacements are analyzed with visual and spectral techniques to quantify impacts from these phenomena. Isotherm displacements are greater in the Slope Sea than the Sargasso Sea, which is evident from filtered high pass isotherms and IW spectral variances. Isotherm spectra indicate the presence of a semidiurnal internal tide, tidal harmonics, and random high-frequency IWs above the caldera. The frequency-dependent normal mode structure of a subsurface duct in the Sargasso Sea is strongly impacted by eddies and IWs. Acoustic path availability near the Atlantis II seamount is investigated using ray theory, which identifies exploitable acoustic paths with minimal boundary interactions. A ray simulation with IW sound speed perturbations demonstrates an increase in exploitable acoustic paths.

THIS PAGE INTENTIONALLY LEFT BLANK

TABLE OF CONTENTS

LIST OF FIGURES

LIST OF TABLES

THIS PAGE INTENTIONALLY LEFT BLANK

LIST OF ACRONYMS AND ABBREVIATIONS

A2	Atlantis II
BI	boundary interaction
BV	Brunt-Väisälä
CTD	conductivity, temperature, and depth
CZ	convergence zone
FFT	fast Fourier transform
GM	Garrett-Munk
IT	internal tide
IW	internal wave
ONR	Office of Naval Research
SONAR	sound navigation and ranging
SSP	sound speed profile
TFO	Task Force Ocean
WBC	western boundary current
XBT	expendable bathythermograph

THIS PAGE INTENTIONALLY LEFT BLANK

ACKNOWLEDGMENTS

I want to express my gratitude to Professor Gemba and Professor Olson for their efforts and support to strengthen this thesis. I'm exceptionally thankful for Mike Cook, who was always available to assist me with my array of MATLAB questions. I owe thanks to Professor Radko for his outstanding instruction and letting me work in his ocean modeling lab as an "adopted student." I greatly appreciate Professor Reeder for setting aside time to discuss his internal wave experience with me, and Dr. Torres at NUWC for the great conversation about his current work and research recommendations.

I was given the privilege to assist in the recovery of the EVM-1B mooring featured in this thesis. During my time aboard the R/V Atlantic Explorer, Professor Andres and Professor Lin made every effort to incorporate me into their fieldwork, answer my questions, and ensure I had a blast. Please accept my deepest gratitude for the experience and your kindness.

I owe a massive thank you to my advisor, Professor Colosi, for inviting me to learn, listen, and participate in this exciting project. I've learned a great deal as his student, and the hours he spent on the whiteboard, MATLAB script, and word processor to enrich my understanding has made all the difference.

This thesis would have been a challenging venture without the unyielding support of my roommates, USW-OC cohort, family, and Max Moore.

THIS PAGE INTENTIONALLY LEFT BLANK

I. INTRODUCTION

A. PHYSICAL SETTING

1. Seamounts

Seamounts are isolated undersea volcanic constructs and are common topographic rises on the seabed of Earth's oceans (Wessel et al., 2010; Yesson et al., 2011). Typical seamount vertical heights range from thousands of kilometers to tens of meters (Wessel et al., 2010). Seamounts and other complex bathymetric features are of high interest to Naval undersea operations. Seamounts can be fatal navigational hazards for submerged vessels underway. Seamounts can physically obstruct acoustic energy and create large shadow zones, which could provide an opportunity for a submerged vessel to evade detection. The upward slopes of seamounts can possess a focusing effect, or amplification, of acoustic energy as rays travel from the feature base towards the summit (Colosi, 2016). Seamounts are hotspots of biological activity, which can elevate ambient noise levels and further complicate acoustic operations (Vlasenko et al., 2018). Seamounts naturally impede current flow, which dissipates tidal energy and facilitates mixing (Vlasenko et al., 2018).

2. New England Seamount Chain

The New England Seamount Chain (NESC) is located off the coast of Massachusetts in the Atlantic Ocean and includes more than 35 topographic features (Shank, 2010). Some seamounts in the NESC occupy over half of the vertical water column, which includes the Atlantis II (A2) seamount, which possesses an approximate vertical height of 3300 meters (Ezer, 1994). The A2 seamount and an adjacent oceanic landform called a caldera are the topographic features of interest in this thesis (Figure 1). A caldera is a volcanic feature which has collapsed near its summit from a violent eruption (National Park Service, 2023). The caldera studied in this thesis is located a few kilometers southeast of A2 and features a vertical height of approximately 3100 meters.

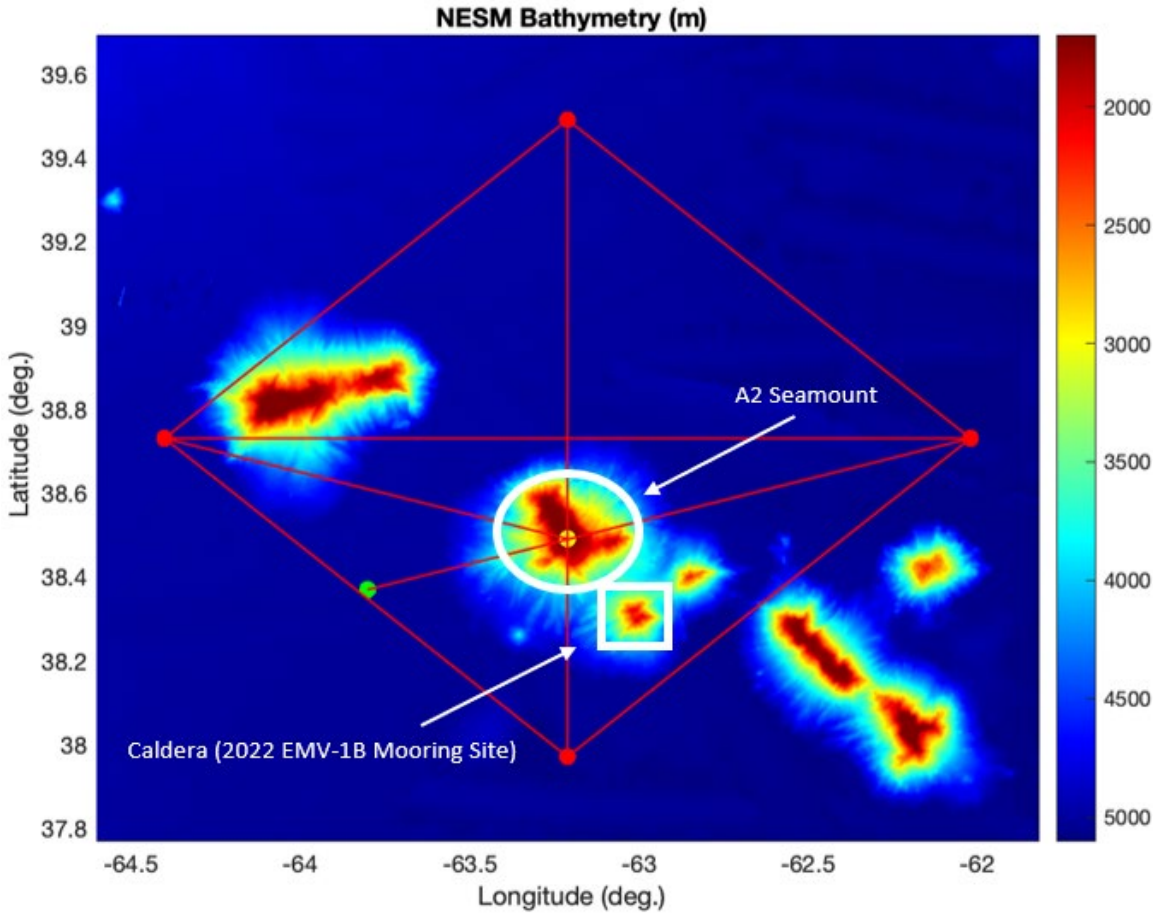

The A2 seamount and caldera discussed in this thesis are distinguished by a white circle and white square respectively. Bathymetric features are shaded in depth, with red colors indicating the peak of a significant topographic rise. Multicolored dots and red lines around the perimeter of A2 mark proposed oceanographic and acoustic equipment locations in support of future NESC experiments and are insignificant to this thesis.

Figure 1. NESC TFO Study Area. Adapted from J. A. Colosi (2022).

3. Gulf Stream and Mesoscale Eddies

The NESC region periodically encounters the meandering Gulf Stream, which is a powerful western boundary current (WBC) in the Atlantic Ocean. The Gulf Stream acts as a frontal boundary between the Sargasso and Slope Seas and features a strong current. The Sargasso Sea resides on the Eastern side of the Gulf Stream, while the Slope Sea is located on the Western side of the Gulf Stream. The Sargasso and Slope Sea possess their own distinct density and sound speed structure. As the Gulf Stream passes over the NESC, the characteristics of the water column surrounding the seamounts will align with the

occupying water mass. The Gulf Stream periodically generates cyclonic and anticyclonic mesoscale eddies which can distort the structure of the upper ocean. Cold-core cyclonic eddies upwell dense seawater to the surface, while warm-core anticyclonic eddies downwell warm surface seawater into the water column. The signature upwelling and downwelling caused by Gulf Stream eddies could be observed in theory by examining the vertical displacement of isopycnal surfaces in the upper ocean over time.

B. INTERNAL WAVE FORMATION AND CLASSIFICATION

1. Internal Waves and Solitons

Internal waves (IWs) are present in most stratified water masses on Earth (Nam et al., 2022). Surface winds and tidal flow over bottom topography are prominent sources of IW generation (Gerkema & Zimmerman, 2008). As IWs propagate, their vertical displacement can cause isopycnal surfaces to oscillate. IWs generate diapycnal mixing (mixing perpendicular to density surfaces), diffuse energy, and create turbulence in the water column as they overturn (Gerkema & Zimmerman, 2008). Sites where IWs are locally generated are known to possess reduced stratification as a result of their associated vertical mixing (Wang et al., 1991). IWs possess maximum spatial scales of kilometers and temporal scales as large as hours (Munk, 1981). IWs are traditionally defined by the frequencies of their restoring forces, which range from the local stratification-driven Brunt-Väisälä (buoyancy) frequency (Equation 1.1), to the Coriolis-driven inertial frequency (Gerkema & Zimmerman, 2008). Near-inertial IWs are sourced from geostrophic adjustment, which occurs when wind driven variability in the mixed layer depth seeks equilibrium (Gerkema & Zimmerman, 2008). IW energy can be intensified by storm systems and surface currents (Nam et al., 2022). Topographically generated IW fields are strongly influenced by the presence of a background current (Vlasenko et al., 2013). Isotherm displacements driven by IW propagation were found to be in phase with depth while a background current was observed (Vlasenko et al., 2013). As IW energy increases, the chances of the wave breaking also increase (Munk, 1981). Vertical velocity shear in the water column can have a greater impact on IW propagation than fluctuations in Brunt-Väisälä frequency (Munk, 1981).

$$N(z) = \sqrt{-\frac{g}{\rho}\frac{d\rho}{dz}} \tag{0.1}$$

Solitons, or internal solitary waves, are strong nonlinear waves which possess large amplitudes (He et al., 2022). Solitons are identified by a single depression or elevation which retains its form while propagating (Gerkema & Zimmerman, 2008). Solitons can originate from internal tides (ITs), which steepen and deform into solitons as they travel away from a generating feature (Akylas et al., 2007; Gerkema & Zimmerman, 2008). The Coriolis force can diminish the number of solitons formed by an IT (Gerkema & Zimmerman, 2008). Solitons may also form if a tidal beam travels upslope and displaces a strong pycnocline (Akylas et al., 2007). A tidal beam can travel considerable distances from the IT-generating topography before disturbing the pycnocline, which generates solitons from the effects of dispersion and nonlinearity (Akylas et al., 2007). Tidal beams and their relationship to IWs are discussed further in an upcoming section.

2. Internal Tides and Tidal Harmonics

Internal tides (ITs), which are also known as baroclinic tides, originate from barotropic tidal flow over bottom topography (Nam et al., 2022). ITs are IWs which propagate at their original tidal forcing frequency (Gerkema & Zimmerman, 2008). Upon contact with a sloped seafloor, previously horizontal barotropic tidal flow acquires a vertical component which displaces isopycnal surfaces (Gerkema & Zimmerman, 2008). As a result of this new vertical component, IT propagation occurs horizontally and vertically from the generating topographic feature (Gerkema & Zimmerman, 2008). Fluctuations in stratification and velocity, alongside the presence of eddies and fronts, can cause ITs to reflect, refract, and assume a more chaotic propagation path (Levine & Richman, 1989).

IT harmonics originate from a nonlinear steepening of the IT, which indicate fluctuating isopycnal displacement magnitudes (Colosi et al., 2013). An experiment investigating IT behavior using a vertical mooring array with oceanographic instruments near a sill in the Laurentian Channel observed that the M2 tidal frequency, alongside the M4 and M6 harmonic frequencies, were the largest measured constituents in the power

spectra for the vertical mooring positioned in closest proximity to the studied bathymetric feature (Wang et al., 1991). M4 and M6 harmonic spikes were not observed in the power spectra for moorings positioned further away from the sill, which implies that these IT harmonics are an artifact of barotropic tidal interaction with topography (Wang et al., 1991).

3. Topographic Diversity and IW Field Impacts

Previous studies have analyzed the IW fields near the Rosemary Bank (Stashchuk et al., 2021) and Anton Dohrn seamounts (Stashchuk et al., 2018; Vlasenko et al., 2018) in the North Atlantic Ocean. These seamounts are 170 kilometers apart and possess distinct geometric differences (Stashchuk et al., 2021). As a result of these differences, these topographic features generate unique IT fields (Stashchuk et al., 2021). An analysis of in-situ and modeled data determined that tidal beams are unlikely to occur from the Rosemary Bank seamount and that tall volcanic cones near the Rosemary Bank seamount's summit are responsible for high frequency IWs in the seasonal pycnocline, while the Anton Dohrn seamount's IW structure lacks these phenomena (Stashchuk et al., 2021). With this determination in mind, the assumption of an identical IW field for separate topographic features is an imprecise practice.

C. TOPOGRAPHY AND HYDRAULIC CONTROL

1. Lee Wave Mechanism

A lee wave mechanism can create IWs, which typically occurs near topographic features with large slopes (Vlasenko et al., 2013). IWs originating from a lee wave mechanism are formed downstream of the topographic feature by substantial supercritical tidal flow (Vlasenko et al., 2013). Supercritical hydraulic states develop when the Froude number (Equation 1.2) is greater than or equal to one (Vlasenko et al., 2013). Supercritical flow is kinetic energy dominant and restricts IW travel against the direction of flow, while subcritical flow is potential energy dominant and allows IWs to freely propagate in any direction (Palmer et al., 2013). Therefore, the presence of supercritical flow indicates that generated IWs cannot travel "upstream" against the direction of existing flow (Palmer et al., 2013). When the tidal forcing slackens and becomes subcritical (Froude number is less

than one), these downstream IWs are released and can propagate upstream (Vlasenko et al., 2013). Experiments conducted near Georges Bank, a portion of the continental shelf in between Cape Cod and Nova Scotia, validated that upstream IW propagation was impossible while the criteria for supercritical tidal flow was achieved (Brickman & Loder., 1993).

$$Fr = \frac{\vec{U}_{tide}}{c_p} \tag{0.2}$$

2. Tidal Beams

A tidal beam is also called a hydraulic jump or tidal bore. Tidal beams are products of a rapid transition between supercritical and subcritical hydraulic states (Equation 1.2), which can be provoked by variabilities in water column depth over bathymetric features and flow direction (Palmer et al., 2013). As a result, tidal beams are expected to travel upward and parallel to the slope of topographic features like seamounts (Vlasenko et al., 2018). Tidal beams have been observed to manipulate the depth of the pycnocline, facilitate diapycnal mixing, and generate IWs (Palmer et al., 2013; Vlasenko et al., 2018). Once a tidal beam interacts with a thermocline, the maximum of Brunt-Väisälä frequency can scatter its energy through internal reflection (Gerkema & Zimmerman, 2008). Vertical gradients of Brunt-Väisälä frequency can also cause refraction of tidal beams (Gerkema & Zimmerman, 2008).

D. ACOUSTIC SIGNIFICANCE OF INTERNAL WAVES

Sound Navigation and Ranging (SONAR) system performance is heavily reliant upon the surrounding sound speed field in the ocean environment. Modern tactical undersea operations rely upon SONAR, and any spatial and temporal variability which impacts the transmission of acoustic signals must be fully understood. IWs are one of the key processes that manipulate acoustic path availability (Colosi, 2016). Along the vertical displacement of density surfaces, IWs are known to scatter acoustic energy into shadow zones and cause waveguides to dilate and compress (Colosi, 2016). The terms waveguide and acoustic duct will be used interchangeably in this thesis. The acoustic impact of vertical

isopycnal displacement from IWs is small, but IW-driven fluctuations in sound speed gradient impact the refraction of acoustic energy as it travels. The relationship between isopycnal vertical displacement (ζ) and the potential sound speed gradient on sound speed fluctuations (δc) is expressed in Equation 1.3 and supports the expectation that IW activity creates a range dependent acoustic field (Colosi, 2016).

$$\partial c(\vec{r},t) = \frac{dc}{dz}_{p} \zeta(\vec{r},t) \tag{0.3}$$

As IW fields propagate in a specific direction, their distortion of isopycnal surfaces will cause the sound speed profile (SSP) to become range dependent (Zhou et al., 1991). As a result of these influences, an acoustic wave propagating through an IW field will experience ray chaos; a phenomenon where available ray trajectories become volatile through fluctuating sound speed initial conditions (Beron-Vera et al., 2003; Brown et al., 2003; Colosi, 2016). An IW field causes an exponential increase in eigenrays and caustics compared to a range-independent sound speed profile (Colosi, 2016). A caustic is a region where a group of acoustic rays converge and intersect (Etter, 2014). Ray chaos can also develop from eddies, surface waves, and bottom roughness (Colosi, 2016).

Modeled or historical environmental data may represent a regional SSP as range independent, which implies that sound speed gradients and duct characteristics will not vary as sound travels. Undersea Naval operations in regions of energetic IW activity could benefit from the analysis of available acoustic paths in the environment to determine which are most reliable as the SSP is manipulated by an IW field. Prior attempts to model range dependent SSPs influenced by IW propagation identify distinct regions of acoustic ray path focusing and defocusing (Baxter & Orr, 1982). Observations of experimental ray trajectories between a source and receiver in range dependent scenarios have demonstrated an acoustic focusing effect if an IW crest is present within the ray propagation path and a defocusing effect for IW troughs encountered in the ray propagation path (Duncan et al., 2018; Gao et al., 2023). This observation of IW crests and troughs has potential to be strategically applied by SONAR operators to increase the probability of detecting a target or evading acoustic detection.

E. NAVAL APPLICATION

The short temporal scale of IW processes and their accompanying acoustic effects could potentially complicate undersea tactical operations. The vertical displacements of powerful IWs, which have been observed in the South China Sea, can impact the ability of a submerged vessel to maintain depth control in the water column (Wang et al., 2022). Modeled hydrodynamic interactions between submarines and solitons within a pycnocline determined that horizontal and vertical forces and torque were intensified when the pycnocline possessed a stronger density gradient (He et al., 2022). The vertical displacement of high energy IW activity is the suspected cause of undesired vertical movement of submerged vessels, which can jeopardize operational limits and elevate risk (Parnum et al., 2017). Any underway platform or seafloor station exposed to IW energy will likely be strained or impacted by their propagation (Wang et al., 2022). With respect to acoustic variability, irregular bathymetry is a common occurrence in every ocean and complex IW fields are likely to exist nearby. The practice of shifting historic or modeled SSP profiles to align with in-situ measurements from expendable bathythermographs (XBTs) or depth excursions will not represent IW-driven fluctuations of waveguides or sound speed gradients. Further, the development of IW alarms or charts indicating known IW activity is excellent for theater level situational awareness but will not aid submerged vessels who need to operate and complete missions in their presence. If a Naval force desires to possess a distinct tactical advantage in undersea acoustic operations, the acoustic variability driven by IW propagation must be well understood to determine whether it can be exploited (and if so, when).

F. OBJECTIVE AND ORGANIZATION

This thesis discusses the tactical use of the ocean environment by investigating the IW field and predicting acoustic path availability in the NESC. This thesis supports research sponsored by the Office of Naval Research's (ONR) Task Force Ocean (TFO) field program in the NESC, which incorporates supporting teams from Scripps Institute of Oceanography, Woods Hole Oceanographic Institution, and the Naval Postgraduate School. In-situ acoustic and oceanographic instruments are planned to be deployed around

the A2 seamount to study the arrival patterns of acoustic signals (Figure 1). A 2022 TFO pilot study for future acoustic research near A2 was conducted, and this pilot study included the deployment of a vertical mooring equipped with oceanographic instruments over the caldera a few kilometers southeast of A2 (Figure 2). The oceanographic data retrieved from the vertical mooring in this 2022 TFO pilot will be analyzed in this thesis. A previously attempted 2022 TFO pilot study over the caldera, which unsuccessfully deployed a vertical mooring with CTD (conductivity, temperature, and depth) and thermistor instruments, inadvertently recorded data along the caldera slope which suggests the presence of an energetic IW field in the water column. This thesis will evaluate the temporal scales of the IW field over a caldera in the NESC, infer the origin of measured IW energy, determine the most reliable acoustic paths between a theoretical source and receiver, and simulate the IW-driven range dependence of these paths in 10-minute intervals.

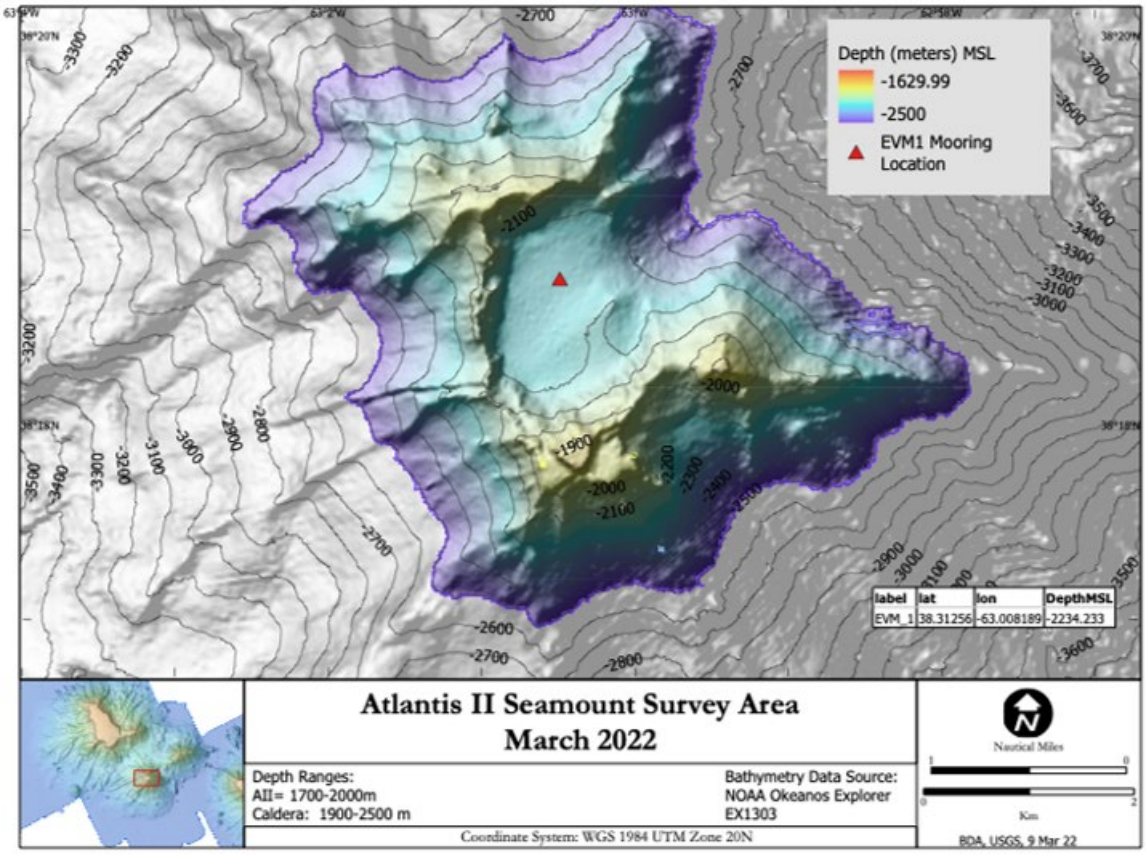

Figure 2. Caldera and EMV-1B Mooring. Source: Chaytor (2022).

The remainder of this thesis will discuss methodology (Chapter II), analyze in-situ oceanographic data (Chapter III), discuss IW-driven variability of the acoustic field (Chapter IV), and provide conclusions and recommendations for future work (Chapter V).

II. DATA ACQUISITION AND PROCESSING

A. VERTICAL MOORING DATA

The 2022 TFO pilot study deployed a single vertical mooring (EMV-1B) with thermistor and CTD instruments to collect oceanographic data over a caldera in the NESC (Figure 2). Vertical moorings are effective in-situ tools which aid researchers in determining the recurrence and persistence of IW activity at a fixed location (Brickman & Loder, 1993). Mooring instruments collected data from 13 June 2022 to 29 August 2022 with a sampling interval of two minutes. Temperature sensors were placed on EMV-1B every 13 meters from 100m–300m, every 30 meters from 300–800 meters, every 50 meters from 800–1000 meters, and every 100 meters from 1000–2200 meters. Salinity instruments (CTDs) collected data for the upper 1000 meters of the water column. Figure 3 is a detailed schematic of the EMV-1B mooring discussed in this study. The EMV-1B did not collect mixed layer (sea surface to 100-meter depth) temperature or salinity data during its deployment, which indicates that an analysis of upper ocean variability may be limited. This is an important consideration for analyzing acoustic paths because shallow water waveguide and surface duct fluctuations are unlikely to be recorded by the mooring. During EMV-1B's data collection, the Gulf Stream meandered over the caldera and induced a water mass shift aloft from the Sargasso Sea to Slope Sea. This frontal boundary passage caused appreciable motion of the vertical mooring and resulted in an additional 200-meter loss of upper ocean sensor coverage in the Slope Sea. To accommodate for WBC flow and inconsistencies with vertical instrument separation in time, isotherms and isopycnals were linearly interpolated onto a fixed depth grid. This interpolation technique has been used in previous studies which utilize vertical moorings to analyze IW behavior (Wang et al., 1991; Colosi et al., 2013; Palmer et al., 2013). Linear interpolation yielded 73 isotherms for the Sargasso Sea water mass and 67 isotherms for the Slope Sea water mass. Isotherms are equally spaced 20 meters apart in depth for both water masses.

Depth-limited and periodically faulty salinity measurements discovered after mooring recovery merit the analysis of isotherm displacements as a proxy for isopycnals. An analysis of interpolated isotherms is a valid scientific approach to study IWs if

isopycnals and isotherms possess nearly identical behavior across depth and time (Wang et al., 1991). A visual comparison of interpolated isotherms and isopycnals within the thermocline with depth demonstrated high coherence for both water masses with isopycnal displacements possessing slightly higher amplitudes (not shown). This thesis assumes that isopycnal and isotherm displacement behavior is identical, and that the vertical displacement of isotherms is due to IW activity alone (Palmer et al., 2013). To elaborate, this thesis ignores the impacts of spice on vertical isotherm displacement, which can have a large influence in the upper ocean. Interpolating between temperature-recording equipment on the mooring benefits from high instrument quantity and low distances separating collecting instruments to resolve variabilities. This thesis assumes that the EMV-1B mooring achieves the desired spatial and temporal resolution to examine the IW field over the caldera (Colosi et al., 2012). Vertical displacement of isopycnal surfaces (or in this thesis, their proxy) is related to perturbations in sound speed (Equation 1.3), which indicates that an analysis of isotherm variability will delineate one factor contributing to acoustic field variability.

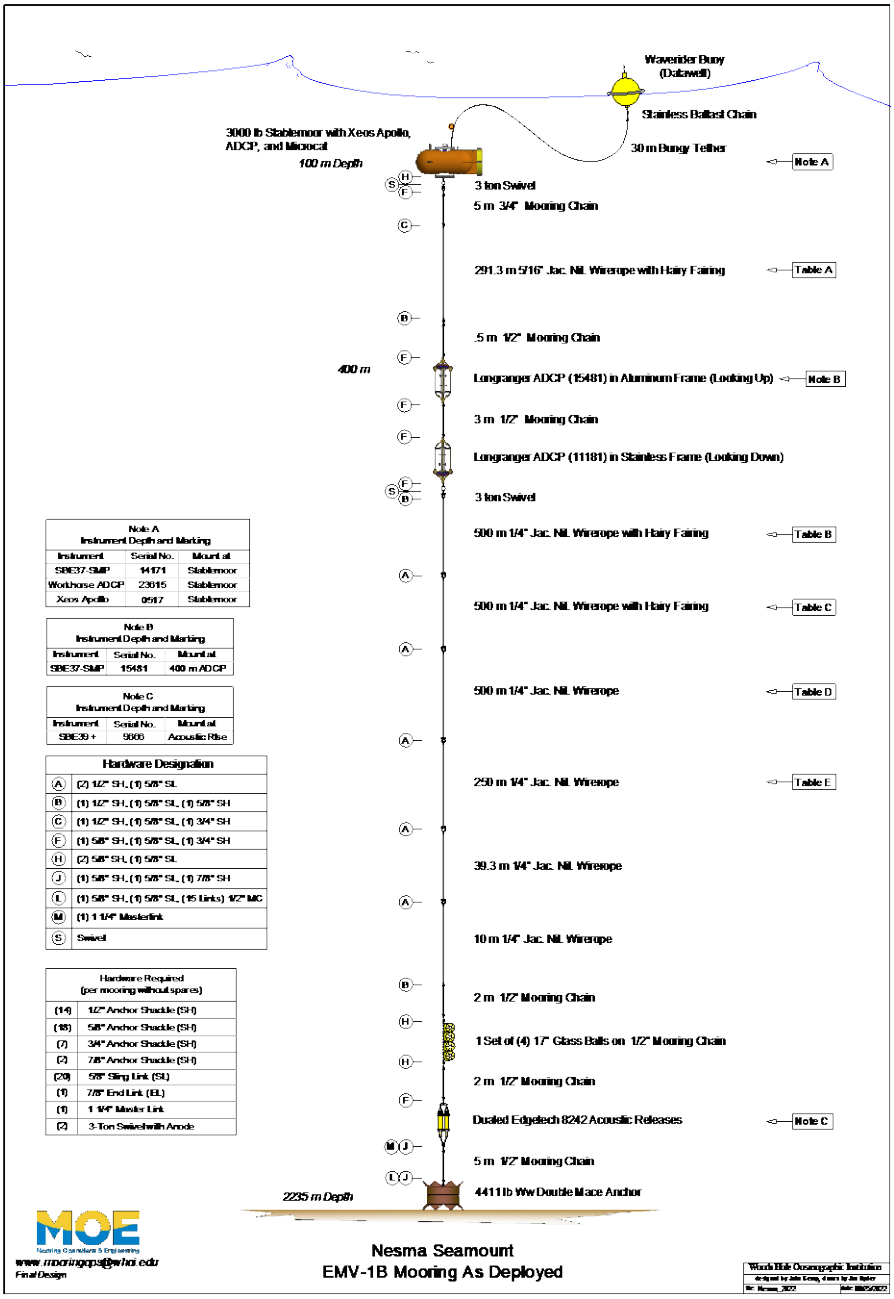

Figure 3. EMV-1B Mooring Schematic. Source: Kemp and Ryder (2022).

Just as potential density is calculated to study isopycnal displacements, potential temperature is used in this thesis to observe adiabatic temperature disturbances (Colosi et al., 2013). A sound speed dataset was derived using the Chen and Millero equation from temperature, salinity, and pressure measurements obtained from the EMV-1B mooring

(Fofonoff & Millard, 1983). During EMV-1B deployment, five full water column CTD casts were conducted in the Sargasso Sea in June of 2022. Six full CTD casts were taken in the Slope Sea during EMV-1B recovery in September of 2022. All CTD casts were collected with a shipboard Seabird 9/11 Plus CTD Rosette. Computed buoyancy frequency (Equation 1.1) and sound speed profiles for CTD cast and EMV-1B averages are compared in Figures 7 and 8.

B. ACOUSTIC RAY THEORY

Available acoustic ray paths near the A2 seamount are approximated using ray theory. This thesis assumes that the IW field present over the caldera is identical to that over the A2 seamount. Although this assumption is probably inaccurate, it is beneficial to analyze ray path tendencies and simulate IW-driven fluctuations as future TFO A2 acoustic research is planned. Ray theory assumes that propagating acoustic energy travels along a ray path at the local sound speed and that diffraction is negligible (Colosi, 2016). Ray theory provides a simple conceptual representation of theoretical acoustic sound propagation and available paths (Colosi, 2016). A convergence of rays is associated with increasing acoustic intensity, while a divergence of rays represents a decrease in intensity (Colosi, 2016). Ray theory struggles to accurately model low frequency acoustic energy and may fail to accurately represent caustic regions (Etter, 2014). The ray theory equations for acoustic refraction (Equation 1.4), position (Equation 1.5), and dispersion (Equation 1.6) assist in calculating horizontal and vertical wavenumber and position for a theoretical ray (Colosi, 2016).

$$\frac{d\vec{k}}{dt} = -\vec{\nabla}\omega(\vec{k},\vec{r}) \tag{0.4}$$

$$\frac{d\vec{r}}{dt} = \frac{\partial\omega(\vec{k},\vec{r})}{\partial k} = c_g \tag{0.5}$$

$$\omega(\vec{k},\vec{r}) = c|\vec{k}| \tag{0.6}$$

Eigenrays are the available acoustic paths which connect a source and receiver (Colosi, 2016). Eigenrays can form a direct path or reflect upon contact with the surface

and seafloor before joining the source and receiver (Etter, 2014). Eigenrays which contact the seafloor, which occur more frequently near topographical features, will reflect with incidence angles equal to their angle of reflection relative to the sloped surface (Colosi, 2016).

THIS PAGE INTENTIONALLY LEFT BLANK

III. OCEANOGRAPHIC ANALYSIS

A. TEMPERATURE, DENSITY, AND SOUND STRUCTURE

Figure 4 captures the 77-day (13 June to 29 August) potential temperature time series collected by the EMV-1B mooring over the caldera. Distinguishable phenomena from this overview of the dataset include the Gulf Stream passage near point A, which separates the Sargasso Sea and Slope Sea water masses (Figure 4). The Sargasso Sea is present over the caldera from mooring deployment at the beginning of the record until the Gulf Stream passage at point A and the Slope Sea is present from the Gulf Stream passage from point A until the end of the record (Figure 4). The Slope Sea portion of the dataset appears to experience two strong downward forcing phenomena at points B and C (Figure 4). Point B is likely caused by a filament of the Gulf Stream near the mooring or downwelling from a strong warm core anticyclonic eddy (Figure 4). Point C, which features a significant loss of upper ocean data, is most likely due to Gulf Stream forcing, which was anticipated to pass over the NESC again after the EMV-1B mooring was recovered in late August (Figure 4).

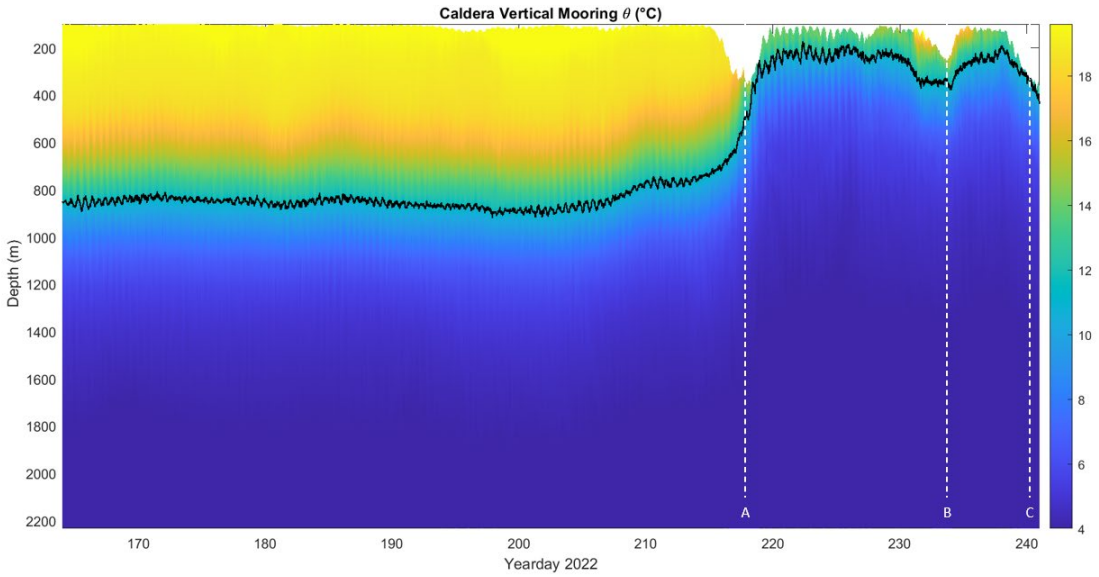

An interpolated 11.29 C isotherm (black) is plotted alongside potential temperature contours to scale measured spatial and temporal fluctuations.

Figure 4. EMV-1B Potential Temperature

Mean temperature profiles with standard deviations of EMV-1B instruments for the Sargasso and Slope Sea are found in Figure 5. Calculated Sargasso and Slope Sea potential density anomaly profiles are found in Figure 6. For Figures 5 and 6, standard deviations of temperature and potential density are displayed horizontally for each measuring instrument attached to the vertical mooring, which is indicated by a blue circle. The upper ocean temperature structure from the surface to 100 meters for both water masses is not measured adequately by the mooring (Figure 5). The Sargasso Sea possesses a well-defined and consistent thermocline ranging from 600–1100 meters while the Slope Sea appears to experience much more variability within a shallower thermocline spanning from 200–450 meters (Figure 5). Below 1500 meters, both Sargasso Sea and Slope Sea temperature profiles appear nearly identical (Figure 5). The Sargasso Sea may possess a seasonal pycnocline near the 100-to-300-meter depth, but this is challenging to determine due to the missing upper ocean data (Figure 6). Substantial temperature and potential density standard deviations near the Slope Sea thermocline suggests that high energy IW activity may be present (Figures 5 and 6) These large Slope Sea standard deviation magnitudes are not observed in the Sargasso Sea, which could be a consequence of increased mixing and residual kinetic energy from the most recent Gulf Stream passage (Figures 5 and 6).

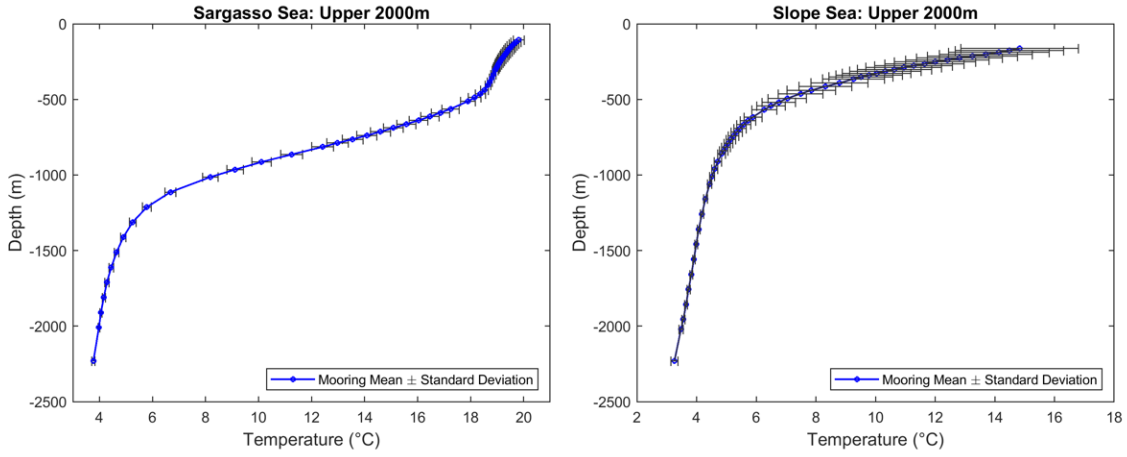

Figure 5. Mean EMV-1B Temperature Profiles

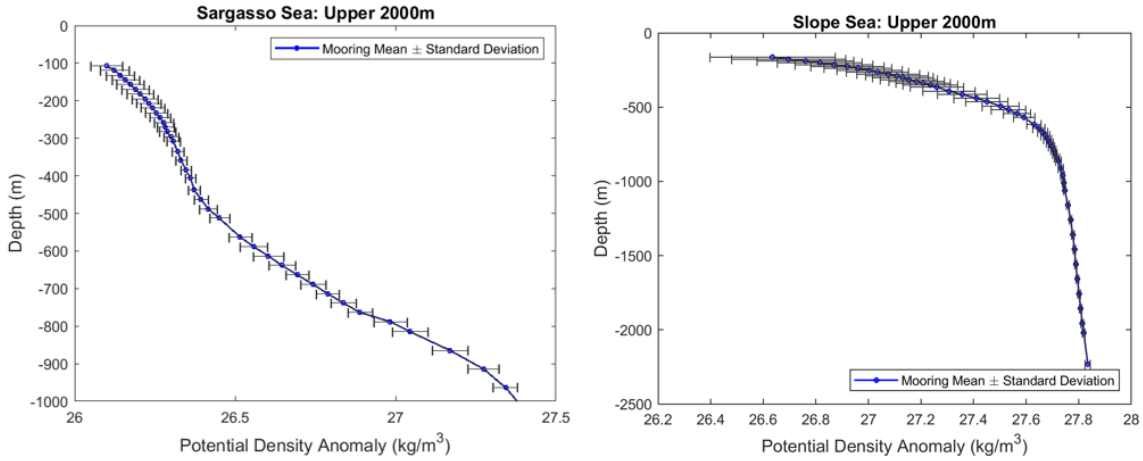

Depth scales in this figure are dissimilar due to inconsistent EMV-1B salinity records.

Figure 6. Mean EMV-1B Potential Density Anomaly Profiles

The mean buoyancy (Brunt-Väisälä) frequency profiles (Equation 1.1) and SSPs with standard deviations for the Sargasso and Slope Seas are found in Figures 7 and 8. The Sargasso Sea SSP features two characteristic ducts: a deep sound channel with an axis located at 1250 meters and a subsurface duct (box H) with an axis near 150 meters (Figure 7). EMV-1B instruments only collect data for the lower half of the Sargasso Sea subsurface duct located at box H but averaged shipboard Sargasso Sea CTD profiles aid in visualizing the full SSP structure (Figure 7). Measured width and length fluctuations of the Sargasso Sea subsurface duct (box H) will be discussed further in the acoustics chapter of this thesis. The Sargasso Sea buoyancy profile possesses a maximum value at around 800 meters, which is typically correlated with the depth of the main pycnocline (Figure 7). The pycnocline observed in Sargasso and Slope Sea potential density anomaly profiles (Figure 6) appear to validate the buoyancy frequency maximum's association with the main pycnocline for both water masses (Figures 7 and 8). The Slope Sea SSP possesses high sound speed variability in the upper 400 meters of the data record, which is also observed in the Slope Sea potential density anomaly and temperature profile (Figure 8). The EMV-1B SSP data for the Slope Sea only depicts a deep sound channel with an axis near 700 meters (Figure 8). Slope Sea CTD SSPs, however, indicate the presence of a small subsurface duct and surface duct structure in the upper ocean which is not measured by the vertical mooring (Figure 8). The Slope Sea's gently sloped buoyancy frequency profile

near its maximum values may be a product of vertical mixing, which could be caused by the Gulf Stream passage or an energetic IW field (Figure 8).

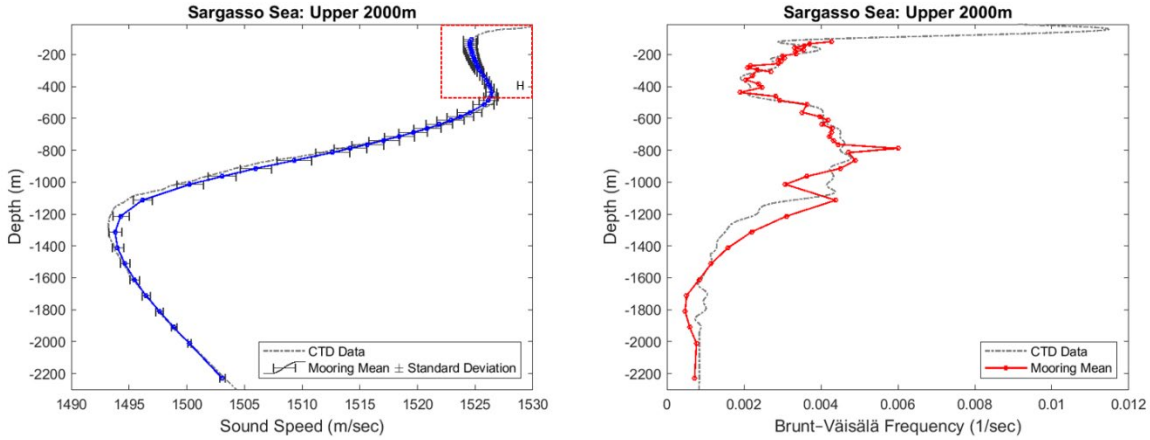

Figure 7. Sargasso Sea Sound Speed and Buoyancy Frequency Profile

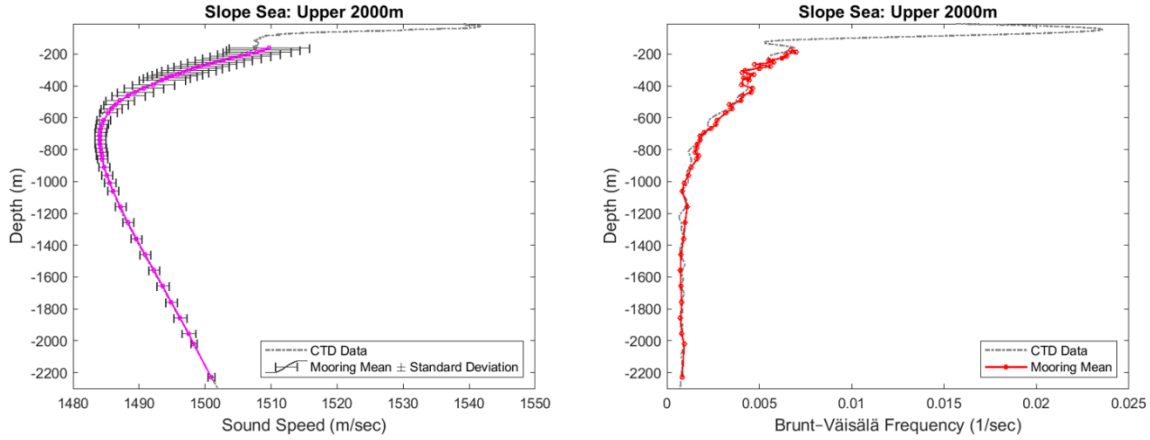

Figure 8. Slope Sea Sound Speed and Buoyancy Frequency Profile

B. ISOTHERM DISPLACEMENT

Interpolated isotherms plotted alongside potential temperature measurements collected by the EMV-1B mooring in the Sargasso and Slope Sea in the upper 1000 meters are shown in Figures 9 and 10. This focused view of Sargasso and Slope Sea isotherm variability in time aids in constructing a more detailed analysis of their influences. Figures 9 and 10 provide a visualization of isotherm oscillations in the Sargasso and Slope

Sea, which appear to be occurring at tidal and supertidal frequencies in both water masses. Points D and G in Figure 9 mark where isotherms appear to be coherently depressed from their mean depth in the Sargasso Sea, which could be caused by a warm core anticyclonic eddy. Points E and F in Figure 9 plot mark where isotherms appear coherently elevated from their mean depth in the Sargasso Sea, which may indicate that the vertical mooring is influenced by a cold core cyclonic eddy at these times. Upon visual inspection of points D, E, F, and G, isotherms do not appear to possess increased amplitudes or a distinguishable change in displacement frequency from the rest of the Sargasso Sea water mass (Figure 9).

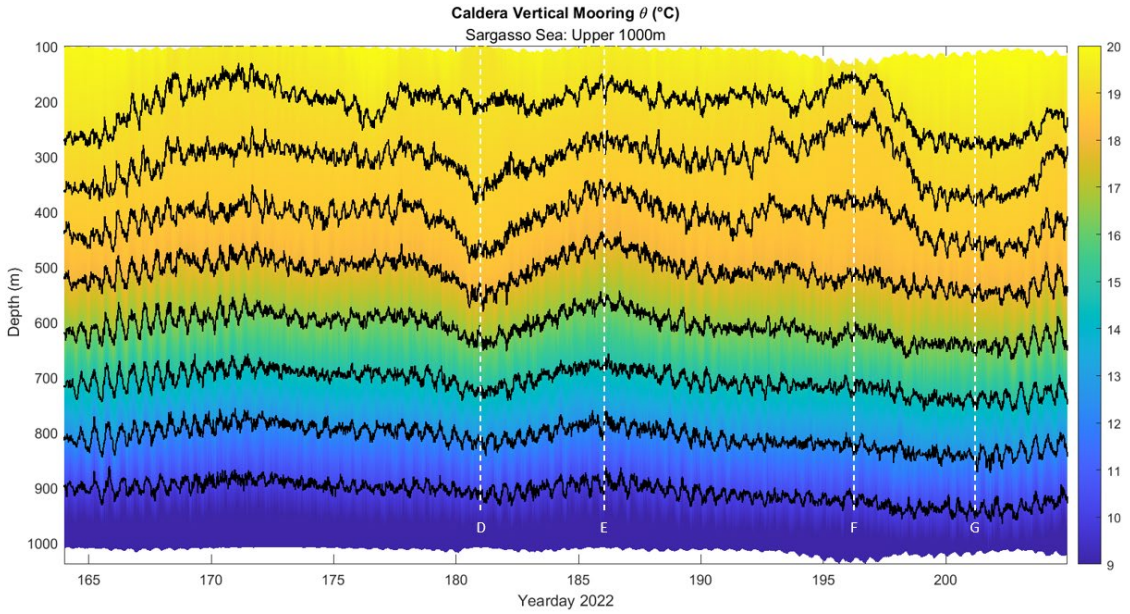

Isotherms (black) plotted from top to bottom: 19.1296 C, 18.8016 C, 18.4565 C, 17.5646 C, 16.0424 C, 14.1039 C, 11.8852 C, and 9.6151 C.

Figure 9. Sargasso Sea Isotherms and Potential Temperature

Points B and C in Figure 10 aid in observing the same points of interest discussed in Figure 4, which are both depression regions of isothermal surfaces in the Slope Sea and likely caused by Gulf Stream or eddy influence (Figure 10). Points B and C on the Slope Sea plot do not appear to feature an increase in amplitude or intensity of vertical isotherm displacement, which is consistent with the isotherm modulation events (points D, E, F, and G in Figure 9) observed in the Sargasso Sea (Figure 10).

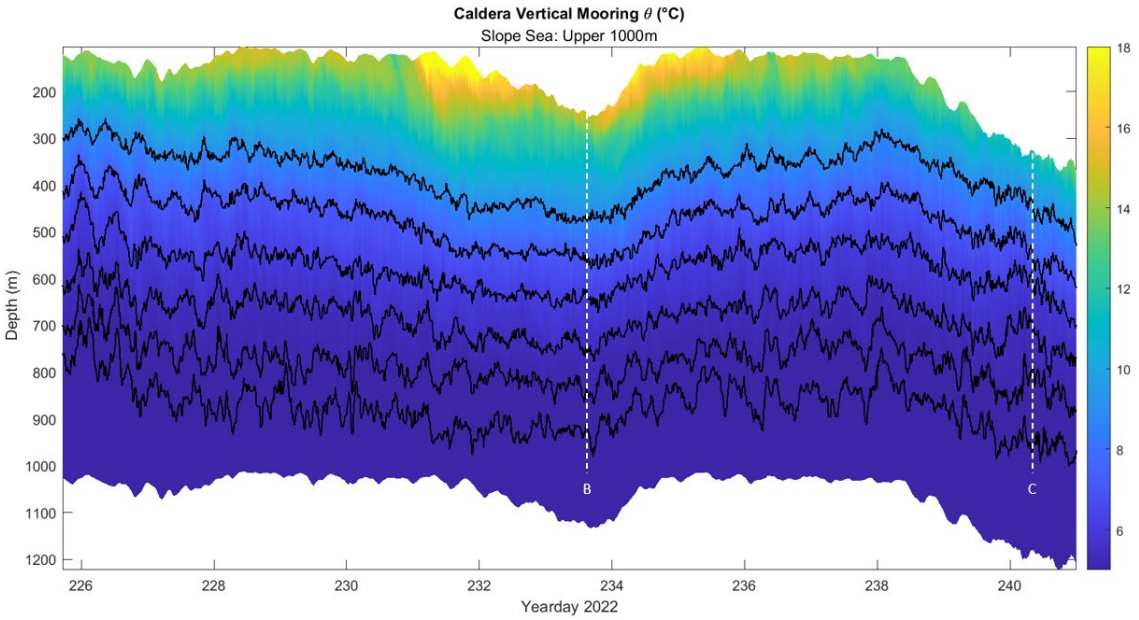

Isotherms (black) plotted from top to bottom: 8.9418 C, 7.2004 C, 6.1149 C, 5.4433 C, 5.0419 C, and 4.7294 C

Figure 10. Slope Sea Isotherms and Potential Temperature

Sargasso and Slope Sea isotherms in the thermocline were low pass filtered to separately investigate their low and high frequency behavior. Isotherms were processed through a low pass Butterworth filter which retained any frequencies lower than ½ of the local inertial frequency (1.2313 cycles per day) for the NESC's latitude. Resulting low pass filtered isotherm displacements are shown on Figures 11 and 12. Unfiltered isotherm displacements are plotted alongside low pass isotherms in Figures 11 and 12 to aid in their comparison. Within the Sargasso and Slope Sea, a semidiurnal IT appears to be the predominant forcing mechanism of isothermal surfaces in the thermocline (Figures 11 and 12). The variations in semidiurnal IT amplitude and higher frequency oscillations within the IT signal, which are consistent in the isotherm records, could be indicative of higher frequency IW energy present above the caldera in the Sargasso and Slope Sea (Figures 11 and 12). Figure 11 annotates the isotherm elevation (points E and F) and depression (points D and G) phenomena which have been previously identified in the Sargasso Sea (Figure 9). Figure 12 also includes the two Slope Sea isotherm depression events (points B and C) which have been previously discussed (Figures 4 and 10). Visually, the presence of eddies

and the Gulf Stream frontal boundary appear to be some of the considerable phenomena responsible for the low-frequency manipulation of vertical isotherm displacements in the Sargasso and Slope Sea. Validation of these phenomena by researching sea surface height and temperature measurements during EMV-1B deployment would aid in confirming the causes of low frequency isotherm distortion. These low frequency, high magnitude isotherm distorting phenomena are sufficiently predicted by ocean forecasting models and their occurrence could provide a distinct tactical advantage for a submerged Naval vessel seeking to exploit their acoustic impacts. Eddies and the Gulf Stream will certainly influence the nearby acoustic field above the caldera, but their presence does not appear to be associated with more intense or tranquil IW propagation.

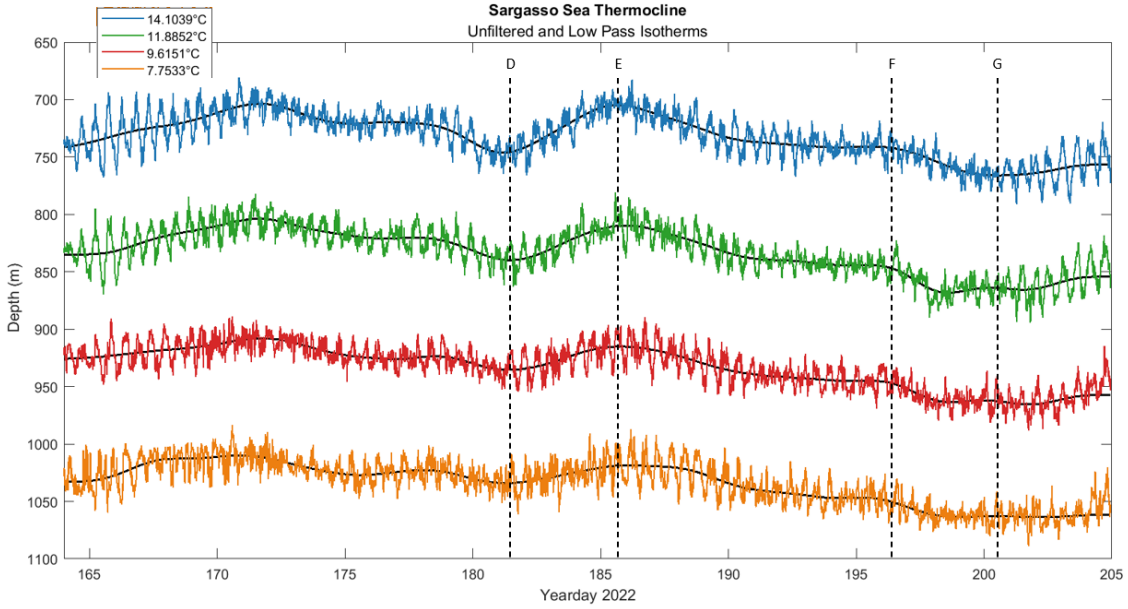

Figure 11. Sargasso Sea Thermocline Low Pass Isotherms

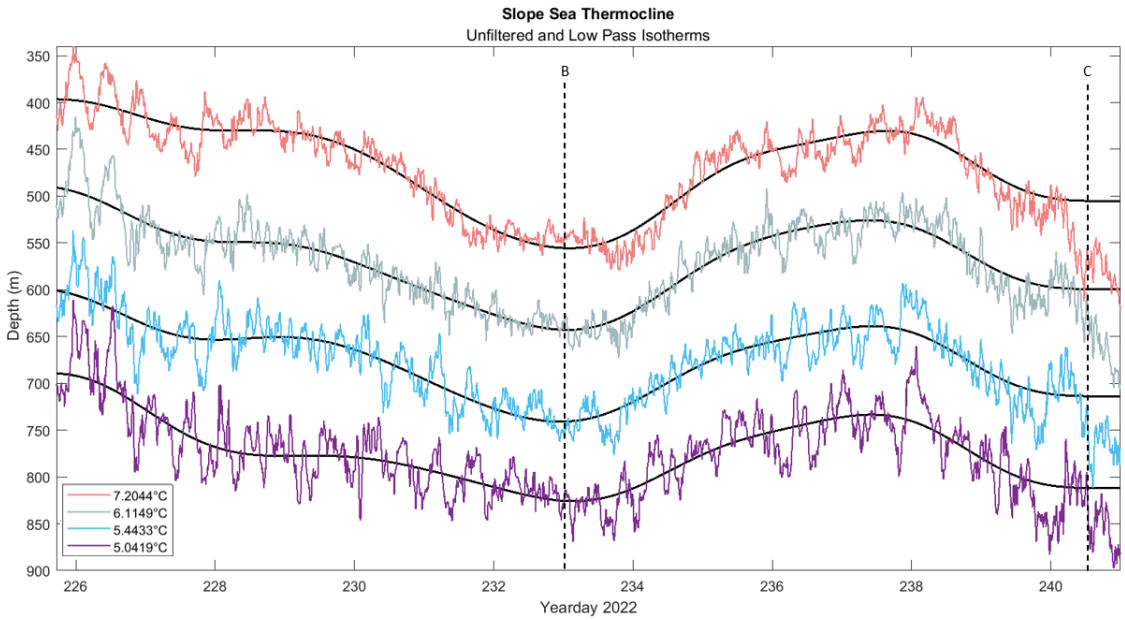

Figure 12. Slope Sea Thermocline Low Pass Isotherms

High pass isotherm displacements were calculated by subtracting unfiltered isotherms from their low pass counterparts and are displayed in Figures 13 and 14. The largest high pass isotherm displacements within a 24-hour period reach 70 meters in the Sargasso Sea and 150 meters in the Slope Sea (Figures 13 and 14), and are clearly caused by the semidiurnal IT. The doubling of vertical isotherm displacement magnitude in the Slope Sea, compared to the Sargasso Sea, is certainly noteworthy (Figures 13 and 14). Time periods of relatively high amplitude high pass isotherm displacement, which were visually identified, are outlined in red boxes (Figure 13 and 14). These periods of energetic IW displacement could be due to an intensification from spring tides, but a more thorough analysis is needed to determine their exact cause.

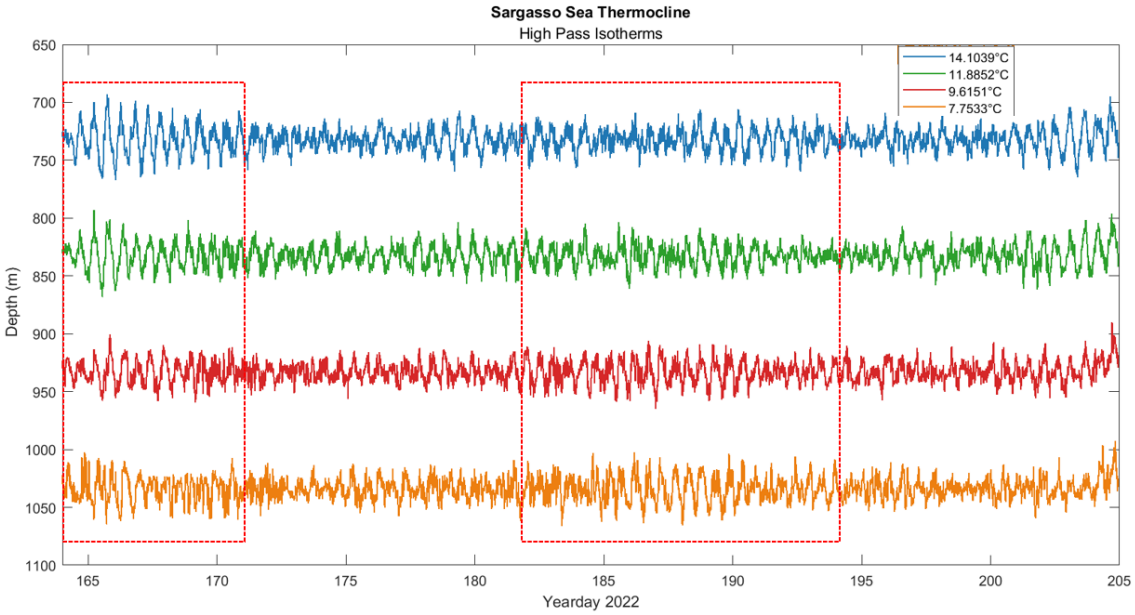

Figure 13. Sargasso Sea Thermocline High Pass Isotherms

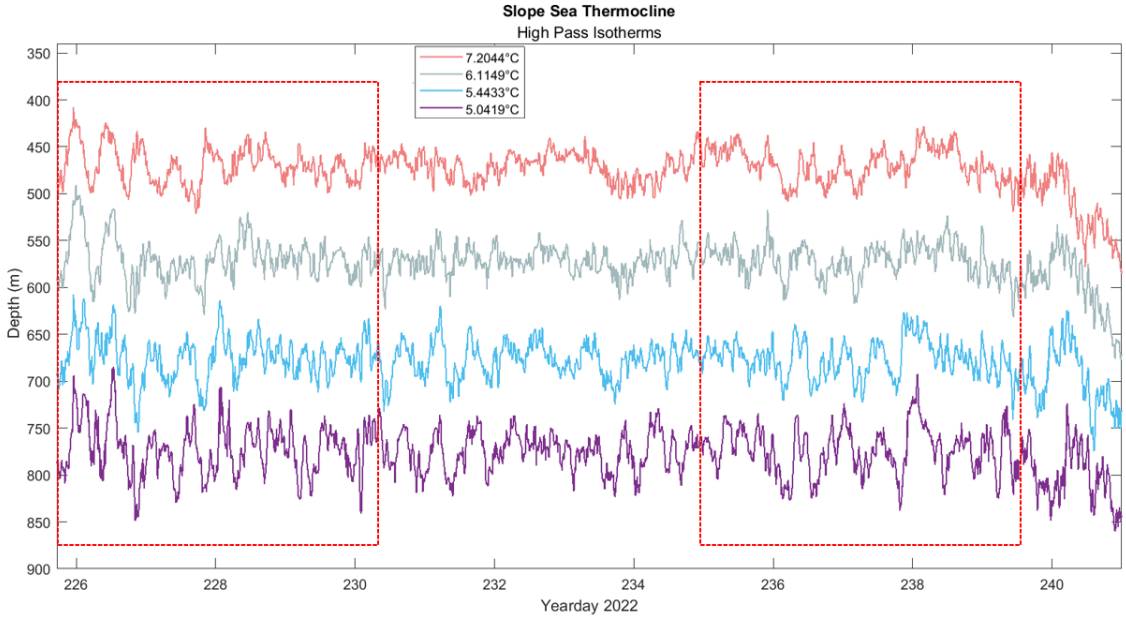

Figure 14. Slope Sea Thermocline High Pass Isotherms

C. BUOYANCY AVERAGED ISOTHERM SPECTRA

The Welch method of fast Fourier transform (FFT) spectral analysis was applied to unfiltered interpolated isotherms in the Sargasso and Slope Sea in order to analyze the

energy and frequency of their vertical displacement. Sargasso and Slope Sea isotherms were averaged into three depth groups of comparable buoyancy frequency. Tables 1 and 2 annotate the isotherm groupings and associated Brunt-Väisälä (BV) frequency averages for each water mass. Isotherm displacement spectra were designed to analyze the frequencies associated with IWs and ITs using a 15-day Hanning window (Figures 15–20).

Table 1. Sargasso Sea Isotherm Spectra Groups

Group and Depth:	Isotherms Averaged:	Mean BV Frequency:
1 (179.8m-306.5m)	1-13	35.7931 cpd
2 (306.5m-1111m)	14-46	56.0074 cpd
3 (1111m-1804.5m)	47-73	11.5985 cpd

Table 2. Slope Sea Isotherm Spectra Groups

Group and Depth:	Isotherms Averaged:	Mean BV Frequency:
1 (349.7m-521m)	1-8	56.7206 cpd
2 (521m-1053.7m)	9-29	24.7868 cpd
3 (1053.7m-1995m)	30-67	11.62 cpd

The Garrett-Munk (GM) IW spectral model, which was empirically developed, describes the variance and temporal distribution of a random internal wave field and assumes an equal distribution of IW energy in all horizontal directions (Munk, 1981). The GM spectral model does not include IT or IT harmonic energy and is known to possess significant errors near abrupt bathymetric features like undersea canyons, continental slopes, and seamounts (Colosi, 2016). Despite these limitations, the GM spectrum provides a good prediction of the energy composition and statistical tool of IW-driven displacement in the frequency domain (Levine & Richman, 1989). This thesis will compare measured

isotherm displacement spectra to the variances predicted by the GM spectral model. The form for the GM displacement spectral shape is expressed in Equation 1.7. Equation 1.8 calculates the anticipated GM IW variance, from the inertial to buoyancy frequency, which is dependent on the resident buoyancy frequency (which changes in depth) where N_o is equal to 3 cycles per hour and ζ_o is equal to 7.3 meters.

$$S_\zeta(\omega) = \langle \zeta^2 \rangle \frac{4}{\pi} f \frac{\sqrt{\omega^2 - f^2}}{\omega^3} \tag{0.7}$$

$$\langle \zeta^2 \rangle_{GM} = \zeta_o{}^2 \frac{N_o}{N(z)} \tag{0.8}$$

The semidiurnal tidal constituents which are expected to be the predominant forcing mechanism of ITs and their harmonics near the NESC are the larger lunar elliptic N2 (1.896 cpd), principal lunar M2 (1.9324 cpd), and principal solar S2 (2 cpd) frequencies. The isotherm displacement spectra for all buoyancy averaged groups annotated in Table 1 and 2 are displayed in Figures 15–20.

1. Sargasso Sea Spectra

Group one in the Sargasso Sea possesses a semidiurnal peak at the S2 tidal frequency and possesses two higher frequency peaks which rise above the estimated GM spectral model at 3.4 cycles per day (cpd) and 3.8 cpd (Figure 15). The 3.8 cpd energy spike is likely the second tidal harmonic of the M2 tide (Figure 15). Group two in the Sargasso Sea possesses a larger semidiurnal peak at the M2 tidal frequency than the Sargasso Sea's first group (Figure 15) and possesses a second IT harmonic peak of the M2 tide at 3.87 cpd (Figure 16). Near-buoyancy high frequency IW energy appears to be more intense in the second Sargasso Sea group (Figure 16) than the first group (Figure 15), which may be due to the second group's proximity to the main pycnocline. Group three in the Sargasso Sea possesses a peak at the M2 tidal frequency and an M2 second harmonic spike with the highest energy of the three Sargasso groups at 3.86 cpd, which is certainly related to the group's proximity to the caldera (Figure 17). The 3.8 cpd M2 tidal harmonic is identifiable in all three Sargasso Sea depth groups, which suggests that the vertical

component of the IT is displacing the entire water column above the caldera. The presence of the M2 second tidal harmonic in all three Sargasso Sea spectra suggests that topographically generated nonlinear phenomena can be observed in all water column depth groups (Figures 15–17). An unexpected result of the Sargasso Sea isotherm spectra is the inconsistency of dominant semidiurnal IT frequencies with depth (Figures 15–17). The mechanics behind this shift from S2 to M2 tidal frequencies in depth are unclear.

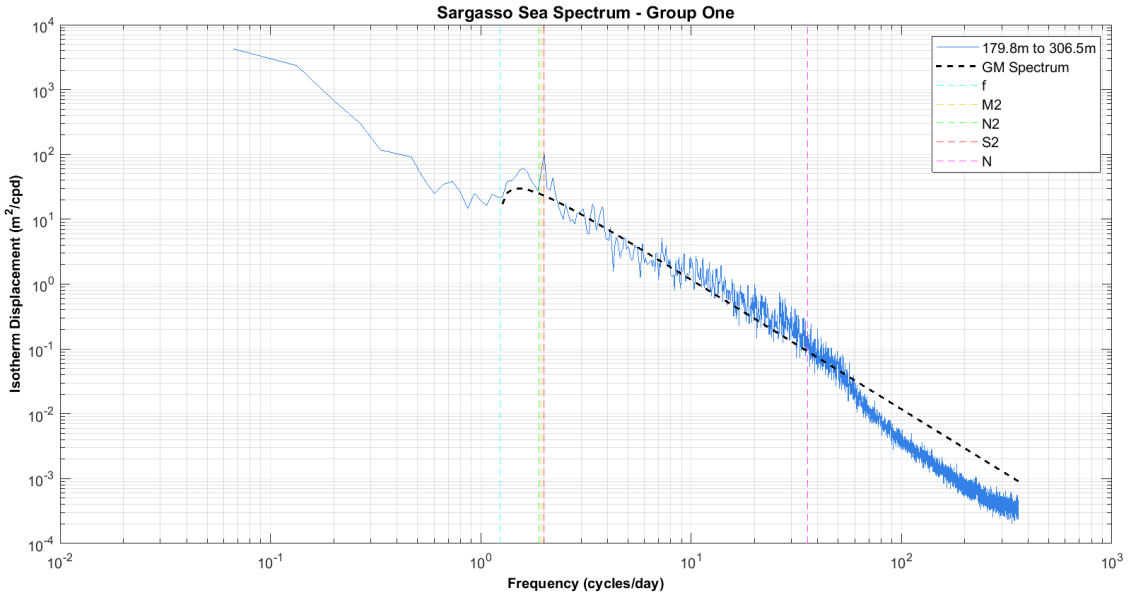

Figure 15. Sargasso Sea Isotherm Spectra (179.8m–306.5m)

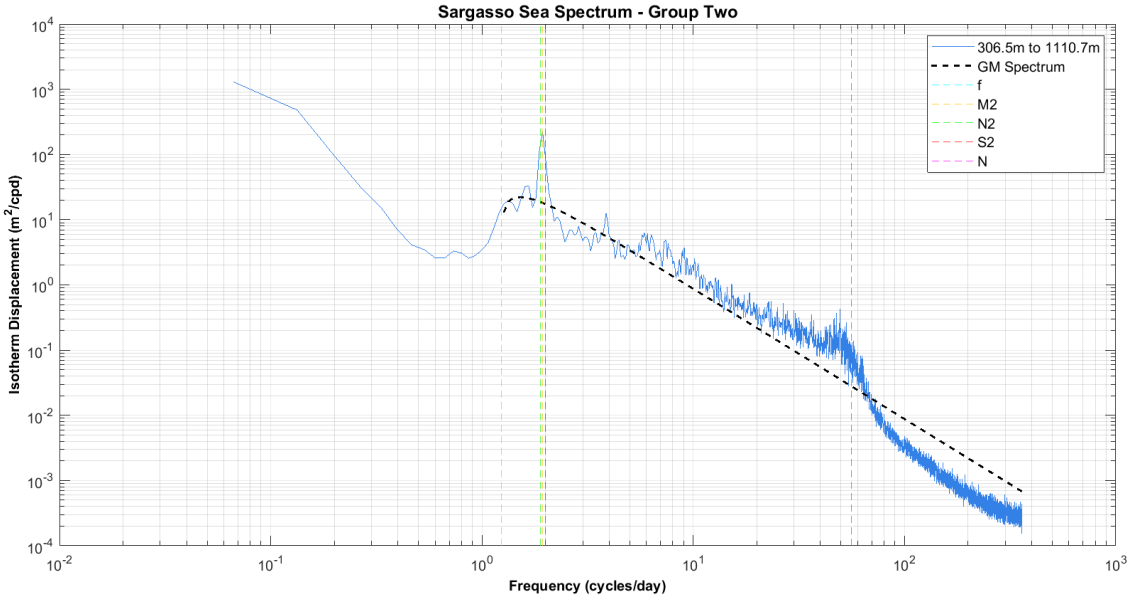

Figure 16. Sargasso Sea Isotherm Spectra (306.5m–1110.7m)

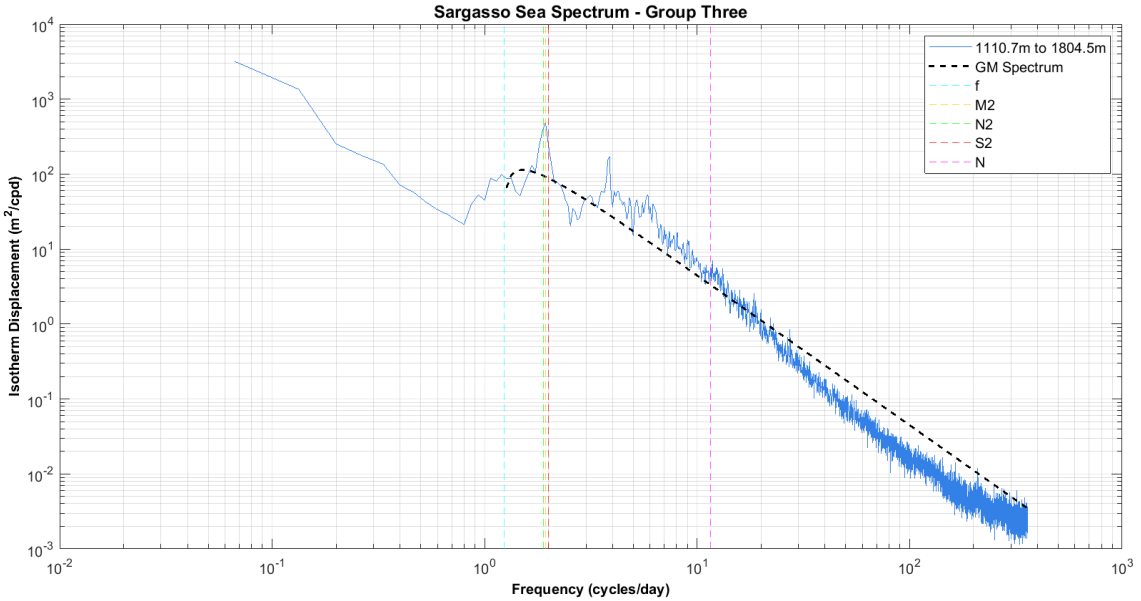

Figure 17. Sargasso Sea Isotherm Spectra (1110.7m–1804.5m)

2. Slope Sea Spectra

Group one in the Slope Sea features a weak spike at the M2 frequency and no other higher frequency harmonics appear to distinguish themselves (Figure 18). However, group one in the Slope Sea appears to possess an energetic field of random IWs across a wide

range of frequencies (Figure 18). Group two in the Slope Sea possesses a more energetic M2 tidal peak than group one and possesses energy spikes at 3.66 cpd, 4.13 cpd, and 6.6 cpd, which could be tidal harmonics (Figure 19). Group three possesses a slightly weaker semidiurnal peak at the S2 frequency, and energy spikes at 3.93 cpd, 4.27 cpd, and 6.13 cpd, which are also possible IT harmonics (Figure 20). The inconsistency of semidiurnal tidal frequencies and IT harmonic peaks with depth, which is a trend observed in both Sargasso and Slope Sea spectra, is a fascinating observation which could be a product of the spectral averaging process.

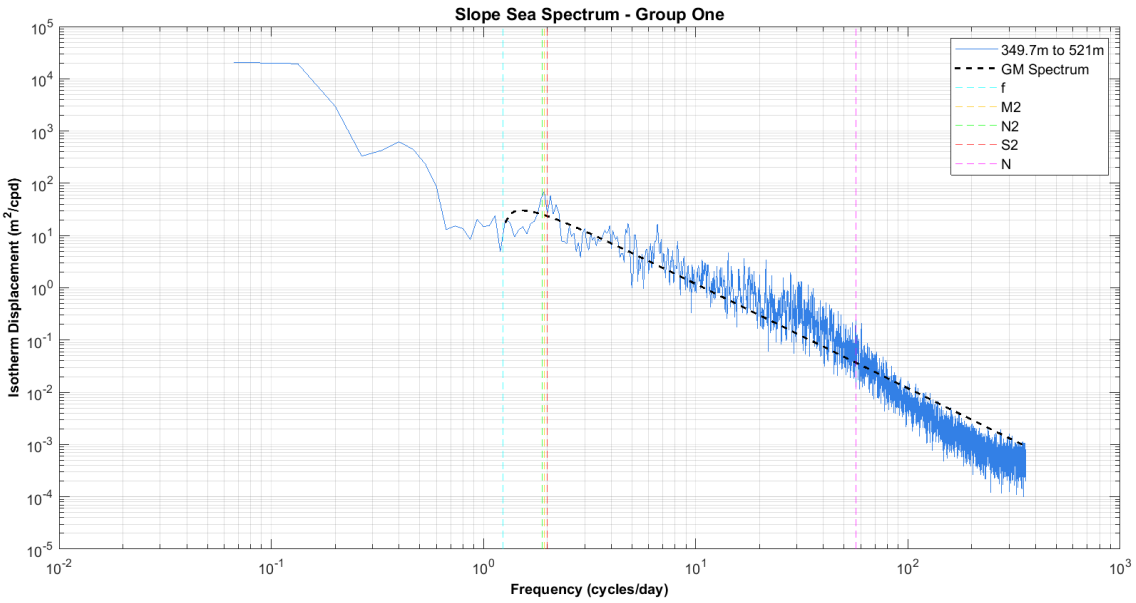

Figure 18. Slope Sea Isotherm Spectra (349.7m–521m)

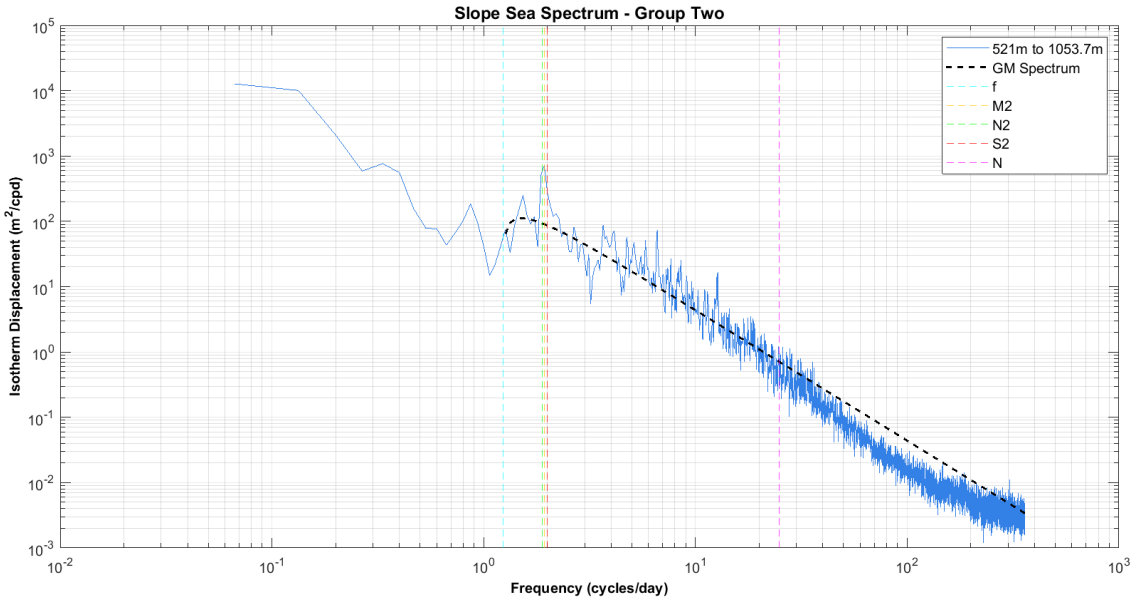

Figure 19. Slope Sea Isotherm Spectra (521m–1053.7m)

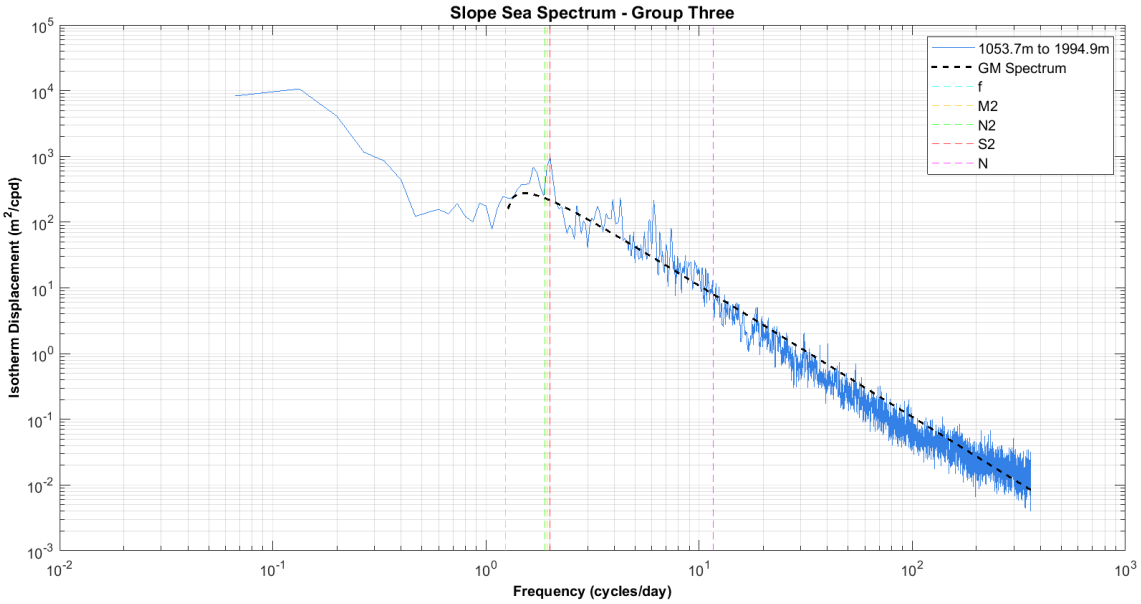

Figure 20. Slope Sea Isotherm Spectra (1053.7m–1994.9m)

Some spectra in the Sargasso and Slope Sea possess abnormal variances at frequencies higher than buoyancy and exceeding traditional IW temporal scales, and this energy may be an indication of nonlinear tidal bore activity in the water mass. This high frequency variance is also observed in seafloor thermistor records from the previously

failed EMV-1B deployment which collected oceanographic data on the slope of the caldera (not shown). Despite meriting continued study, this high frequency energy presence will not be investigated further in this thesis. Table 3 contains the semidiurnal IT variance, measured with an equal bandwidth, and the dominant semidiurnal tidal frequency present in the Sargasso and Slope Sea spectra for each isotherm group. Table 3 demonstrates an increase in IT isotherm displacement with depth in the Sargasso and Slope Sea. Table 4 contains the variance from all IW energy (ranging from the inertial to buoyancy frequency and including ITs) in the spectra for each isotherm group. Table 4 suggests that the deepest isotherm groups in the Sargasso and Slope Sea possess considerably higher IW energy than other groups, which is similar to the IT energy trend in Table 3.

Table 3. Measured Semidiurnal IT Energy Variance

Water Mass:	Group:	Tidal Constituent:	Variance (m^2):
Sargasso	1	S2	18.6041
Sargasso	2	M2	32.4089
Sargasso	3	M2	102.7857
Slope	1	M2	16.8501
Slope	2	M2	122.5269
Slope	3	S2	186.2051

Table 4. Measured IW Energy Variance

Water Mass:	Group:	Variance (m^2):
Sargasso	1	93.4263
Sargasso	2	88.3775
Sargasso	3	387.9403
Slope	1	93.0186
Slope	2	402.8294
Slope	3	880.8363

3. Theoretical and Measured Isotherm Variance

Table 5 illustrates the difference between spectral IW isotherm displacement variances, with the predominant semidiurnal tidal energy removed for each group, and estimated GM spectrum variances (Equation 1.8) expressed as a ratio. Measured isotherm variance includes the energy present in tidal harmonic frequencies, which is not accounted for in the GM spectrum. A ratio of in-situ to theoretical GM variances demonstrates the amount of energy contributed into isotherm displacement by nonlinear IW activity, and compares the displacements recorded over the caldera to empirical IW energy levels worldwide. Of note, isotherm groups with higher IT and IW variances (Tables 3 and 4) also possess a larger measured to theoretical variance ratio (Table 5).

Table 5. Ratio of Measured and Theoretical GM Energy

Water Mass:	Group:	In Situ/GM:
Sargasso	1	0.6980
Sargasso	2	0.8170
Sargasso	3	0.8620
Slope	1	1.1260
Slope	2	1.8108
Slope	3	2.1037

IV. ACOUSTIC ANALYSIS

A. SARGASSO SEA SUBSURFACE DUCT VARIABILITY

The time and range dependent fluctuations of acoustic ducts can complicate SONAR performance. An analysis of SONAR system performance is initiated with the identification and prediction of ocean acoustic paths. The acoustical and statistical properties of a signal are determined by how an acoustic path samples the ocean environment. This chapter is focused on identifying acoustic paths in the Sargasso and Slope Sea and examining their time dependence as the ocean sound-speed field evolves.

An ocean feature which substantially impacts path availability is the large sub-surface duct present in Sargasso Sea water and observed in EMV-1B data and shipboard CTD observations (Figure 7). The Slope Sea SSP (Figure 8) features a weak subsurface duct with an axis near 160 meters, which is evident in shipboard CTD data but is not measured in any manner by EMV-1B instruments. An analysis of the fluctuations of the Sargasso Sea subsurface duct is discussed here because the waveguide was partially sampled by the EMV-1B mooring. In order to determine the spatial and temporal fluctuations of this subsurface duct, its missing upper half was interpolated onto the EMV-1B's sound speed timeseries of the lower half using the CTD-averaged shape of the Sargasso Sea SSP. As a result of this interpolation, the upper half of the Sargasso Sea subsurface duct is assumed to be constant and independent of time. Therefore, the variability of this subsurface duct serves as a rough approximation and likely portrays a small portion of the waveguide's true structural dynamics during EMV-1B deployment. Two important quantities that define the strength of a duct are the vertical spatial extent (Δz) and the depth of the sound speed minimum (Δc).

Figure 21 demonstrates the duct width (Δc) and length (Δz) of the Sargasso Sea subsurface duct in time determined by CTD profile interpolation and EMV-1B data. Points D, E. F, and G in Figure 21 are the periods associated with an observable depression (points D and G) or elevation (points E and F) of isothermal surfaces in the Sargasso Sea and identified in Figure 9. Both duct length and width measurements demonstrate a notable

variability of the subsurface duct at scales of days or less (Figure 21). Most short-term (scales of hours) duct width (Δc) oscillations appear to possess a 1 m/sec difference from peak to trough (Figure 21), while short term duct length (Δz) oscillations yield an 80-meter difference from peak to trough. These oscillations seem to occur with a semidiurnal periodicity, which is consistent with the dominant semidiurnal IT variance seen in the Sargasso Sea isotherm spectra (Figures 15–17). Point D, an isotherm depression event, aligns with the maximum value of duct width and duct length, which suggests that the forcing mechanism responsible for the isotherm depression could also be causing an immense length and width dilation of the subsurface duct (Figure 21). At point D, duct width appears to double in size from its EMV-1B interpolated average (Figure 21). Point E, an isotherm elevation event, aligns with a relative minimum in duct width and length, which suggests that isotherm displacement and subsurface duct variability may be correlated (Figure 21). Point F is associated with a slight increase in duct width but no distinguishable change in duct length. Point G does not appear to be correlated with any significant changes in duct width or length. The regions of high intensity isotherm displacement in Figure 13 do not appear to be related with more energetic duct length or width fluctuations.

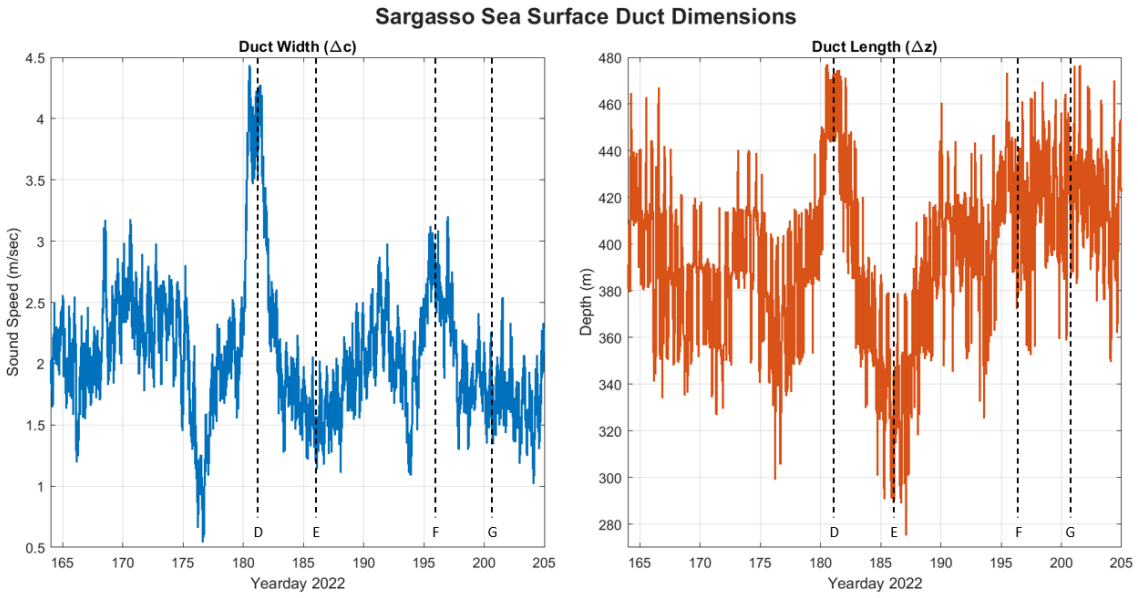

Figure 21. Sargasso Sea Subsurface Duct Width and Length

For a specific frequency (f), the maximum mode number (N_{max}) supported within an acoustic duct comprised of a combination of positive and negative sound speed gradients, or two turning points (γ=0.5), with a specific length (Δz) and width (Δc) can be derived from Equation 1.9. With respect to the relationship between N_{max}, Δz, and Δc, ocean acoustic waveguides are limited to a small range of acoustic modes by their typical length and width scales (Equation 1.9). Any fluctuations in maximum mode number within an acoustic duct is expected to considerably impact ducted acoustic energy and available paths. Generally, an increase in N_{max} within a waveguide is associated with a higher likelihood of acoustic trapping, which could provide an increased probability of acoustic detection. Equation 1.9 also expresses how perturbations of a waveguide's duct length (Δz) will have a greater impact than duct width (Δc) on maximum mode number and acoustic trapping.

$$N_{\max} = f\frac{\Delta z(4\sqrt{2})\sqrt{\Delta c}}{3\sqrt{1500^3}} + 0.5 \tag{0.9}$$

Figure 22 demonstrates the variability of the maximum mode number within the Sargasso Sea subsurface duct for a 250 Hz acoustic signal (Equation 1.9). Points D, E, F, and G in Figure 22 are the Sargasso Sea isotherm depression and elevation events observed in Figure 9 and referenced in Figure 21. Points D, E, F, and G, with respect to the maximum mode number plot, align with the observed maxima and minima observed in the duct width and length plots (Figure 21) as a product of their relationship expressed in Equation 1.9 (Figure 22). Excluding any anomalous spikes and dips, typical mode number fluctuations appear to possess a semidiurnal periodicity and typically feature two modes separating crests and troughs (Figure 22). This semidiurnal oscillation, which is also expectedly present in the duct width and length plots (Figure 21), implies that maximum mode number perturbations of the Sargasso Sea subsurface duct could be related to IT and IT harmonic displacement over the caldera (Figure 22).

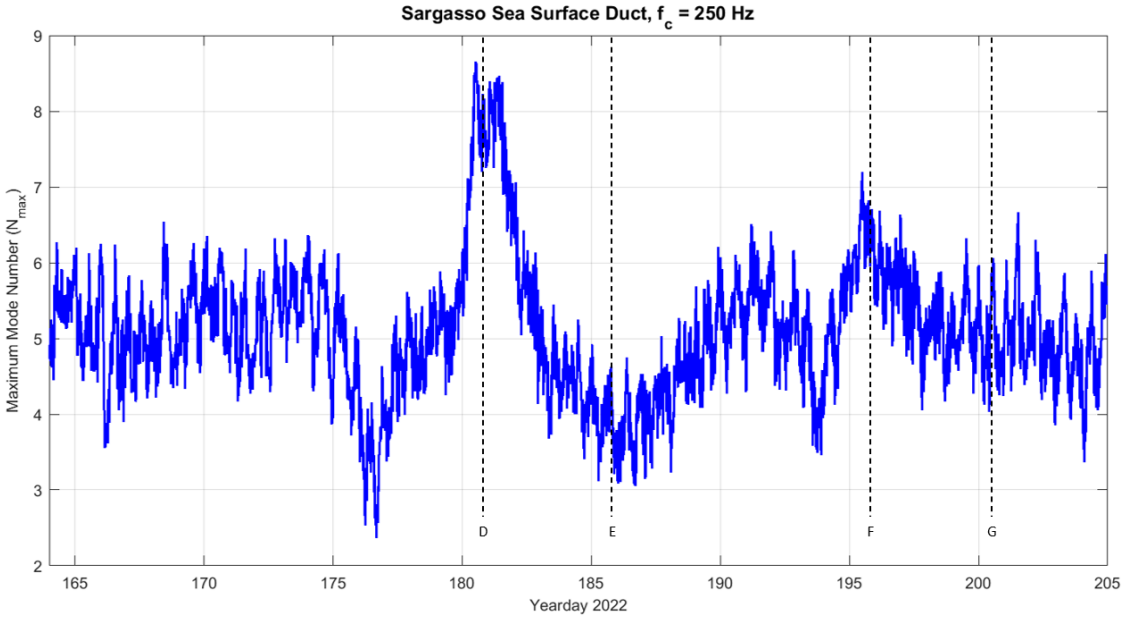

Figure 22. Sargasso Sea Subsurface Duct Maximum Mode Number

B. ACOUSTIC PATHS AND RAY CHAOS

In the previous section, an analysis of mode trapping in the Sargasso Sea subsurface duct was performed because acoustic trapping is associated with path availability, and it aids in predicting differences in frequency. Generally, higher frequency acoustic signals are more readily trapped than lower frequencies.

In this section, an acoustic path analysis using ray theory is implemented in order to examine the entire sound-speed waveguide, consider bathymetric interaction, and simulate IW effects. This path analysis does not treat frequency dependence. Eigenrays were calculated for a theoretical source and receiver at specific depths in the Sargasso and Slope Sea in order to determine available range independent acoustic paths in the two-dimensional plane and simulate IW-driven range dependent ray chaos in ten-minute intervals. CTD-averaged SSPs were used as the baseline sound structure for each water mass. A2 bathymetry was integrated into ray path computations and low pass filtered to simplify bottom bounce interactions between acoustic rays and the A2 seamount slope (Figure 23). The A2 slope, derived from Figure 23, impacts how acoustic energy is reflected upon contact with A2 and separately provides an indication of the trajectory of

tidal beams if their formation conditions are met. In each acoustic simulation, the source is always positioned 60 kilometers away from A2 to allow at least one convergence zone (CZ) propagation path to reach the receiver (Figure 24). The source depth is modified in order to exploit different waveguides and study resulting ray path availability. The receiver is positioned in one of two places for each simulation: over the summit of A2 (61 km away from the source) or on the opposite side of A2 (130 km away from the source, which places the seamount in between the source and receiver). The distances between the source and receiver, alongside low pass bathymetric filtering, provide a simplified two-dimensional and omnidirectional representation of propagation variability near A2 and mimics the action plan for future TFO NESC acoustic research.

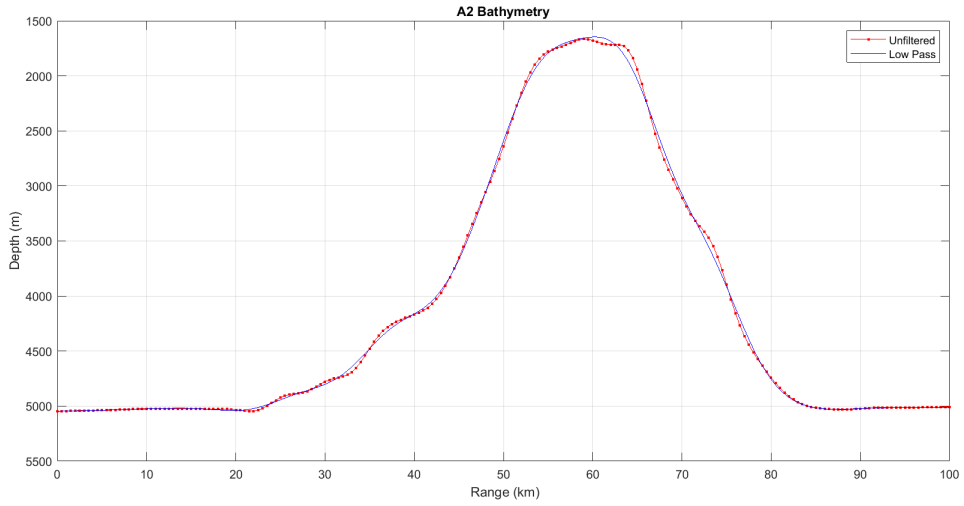

Figure 23. Atlantis II Seamount Bathymetry

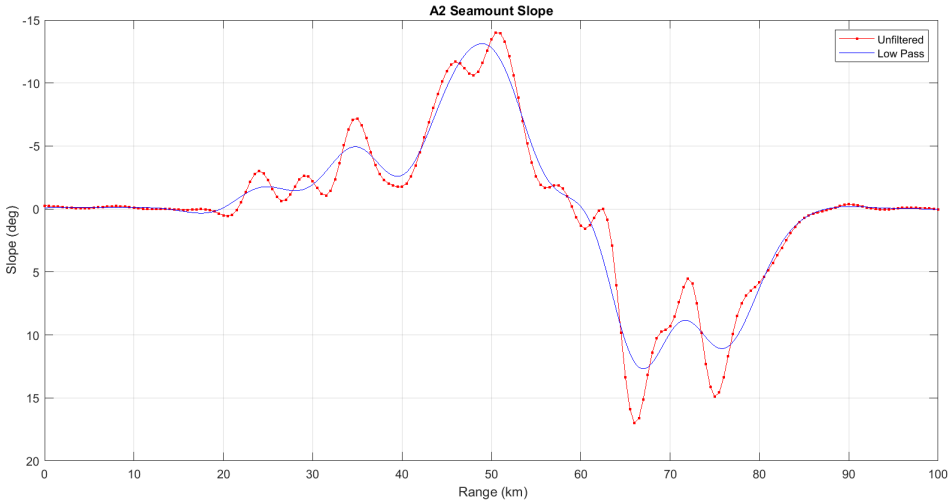

Figure 24. Atlantis II Seamount Slope

1. Range Independent Acoustic Propagation

Eigenrays are color coded by the degree which rays interacts with the sea surface and seafloor, and each instance of contact and reflection is referred to as a boundary interaction (BI) in this thesis. Rays with minimal BI (shaded light green), which include ducted rays with no BIs, are assumed to be the most reliable acoustic paths for target detection within the source and receiver tactical scenario. Rays with moderate BI are shaded yellow, and rays with more significant BI are shaded red. To reiterate, this analysis is focused on the likelihood of receiving a long-range acoustic signal originating from the source or receiver. A ray classified as possessing one BI indicates that the eigenray could have interacted once at a maximum with the sea surface and seafloor. Rays with two or more BIs are more likely to deteriorate from energy loss and scattering as they repeatedly interact with environmental boundaries, which makes them more unreliable for signal reception and processing. This color identification system is implemented for all range independent acoustic path figures in this chapter. Range dependent acoustic paths use a separate color organization to demarcate their differences. In pursuit of clarity for the reader, range dependent and independent eigenrays are assumed to propagate from left to right while each figure is discussed.

The range independent acoustic paths and eigenray receive angles for the Sargasso Sea with the source and receiver at a 250-meter depth and separated by a range of 61 kilometers are shown in Figure 25. The Sargasso Sea's most reliable range independent paths at a 61 km range (annotated in green) include direct path rays refracted within the Sargasso Sea subsurface duct (Figure 7) and a collection of bottom bounce rays which interact with the seafloor at a shallow angle of incidence to the seafloor tangent line before encountering the A2 slope (Figure 25). For a Sargasso Sea source and receiver at a 130-kilometer range and depth of 250 meters, subsurface ducted energy and CZ rays that travel over A2 are the most reliable acoustic paths (Figure 26). The rays which gently reflect off the seafloor in the 61-kilometer scenario (Figure 25) disappear at a 130-kilometer range, which is a product of A2's physical obstruction of acoustic signals (Figure 26). Both Figures 25 and 26 portray A2's interference of acoustic energy propagation, and how a single BI on A2's slope can increase a ray's likelihood of experiencing more BIs due to topographic acoustic focusing.

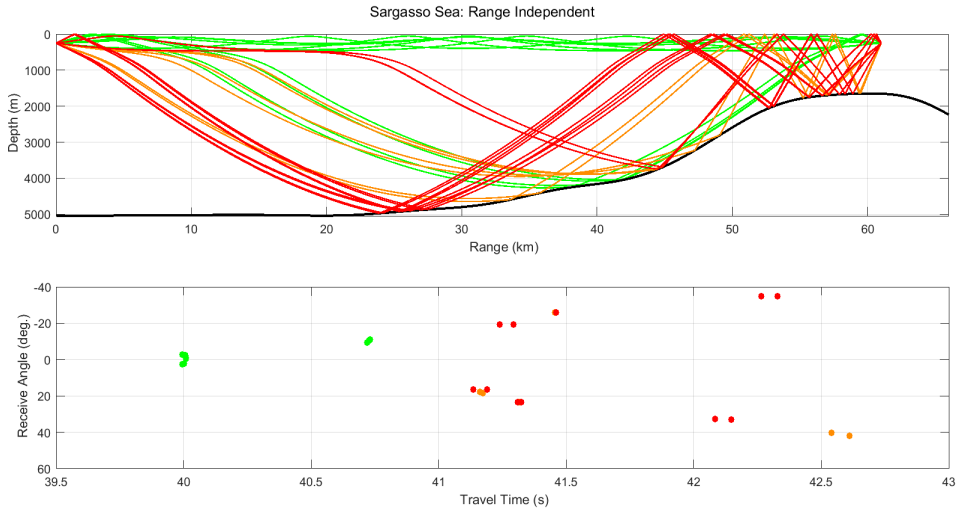

Eigenray paths (top) and their respective source receive angles (bottom) are categorized by their number of boundary interactions (BIs). Green eigenrays indicate one or no BIs, yellow eigenrays indicate two BIs, and red eigenrays indicate three or more BIs.

Figure 25. Sargasso Range Independent Rays (SD = 250m, R = 61km)

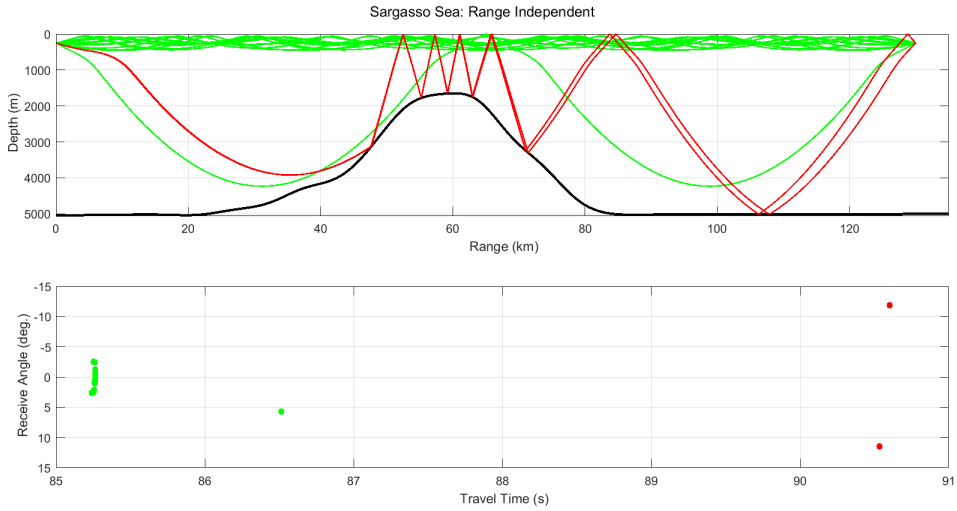

Eigenray paths (top) and their respective source receive angles (bottom) are categorized by their number of boundary interactions (BIs). Green eigenrays indicate one or no BIs, yellow eigenrays indicate two BIs, and red eigenrays indicate three or more BIs.

Figure 26. Sargasso Range Independent Rays (SD = 250m, R = 130km)

The range independent acoustic paths and eigenray receive angles for the Slope Sea with the source and receiver at a 250-meter depth and 61-kilometer range are demonstrated in Figure 27. The most reliable acoustic paths in the Slope Sea 61-kilometer scenario include ducted rays refracted by the deep sound channel (Figure 8) and a CZ path which nearly grazes the leftward slope of A2 (Figure 27). No rays appear reliable if they possess a seafloor BI in the Slope Sea at a 61-kilometer range (Figure 27), which contrasts with the 61-kilometer acoustic paths in the Sargasso Sea (Figure 25). Figure 28 portrays the Slope Sea range independent acoustic paths at a 130-kilometer range and indicates that CZ rays are the most reliable paths for long-range acoustic detection, which is consistent with the Slope Sea 61-kilometer scenario (Figure 28) and Sargasso Sea 130 kilometer scenario (Figure 26).

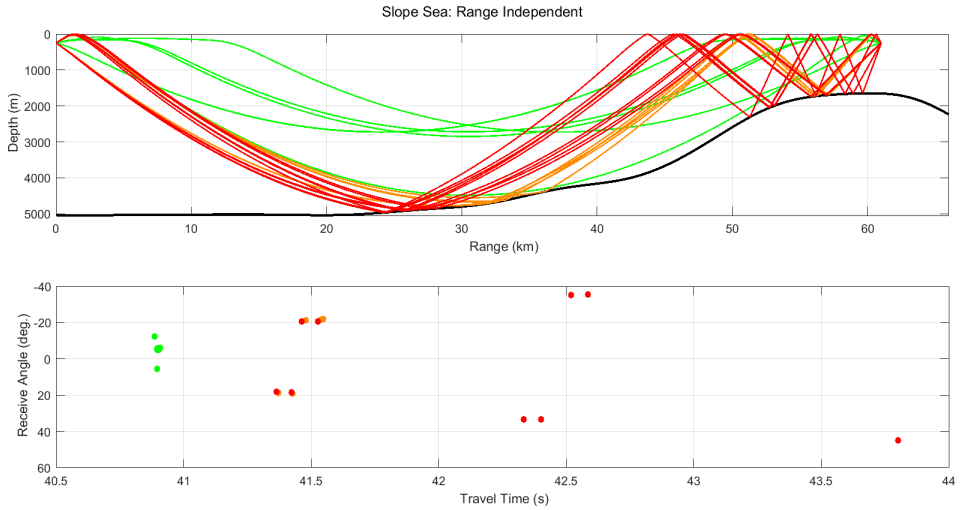

Eigenray paths (top) and their respective source receive angles (bottom) are categorized by their number of boundary interactions (BIs). Green eigenrays indicate one or no BIs, yellow eigenrays indicate two BIs, and red eigenrays indicate three or more BIs.

Figure 27. Slope Range Independent Rays (SD = 250m, R = 61km)

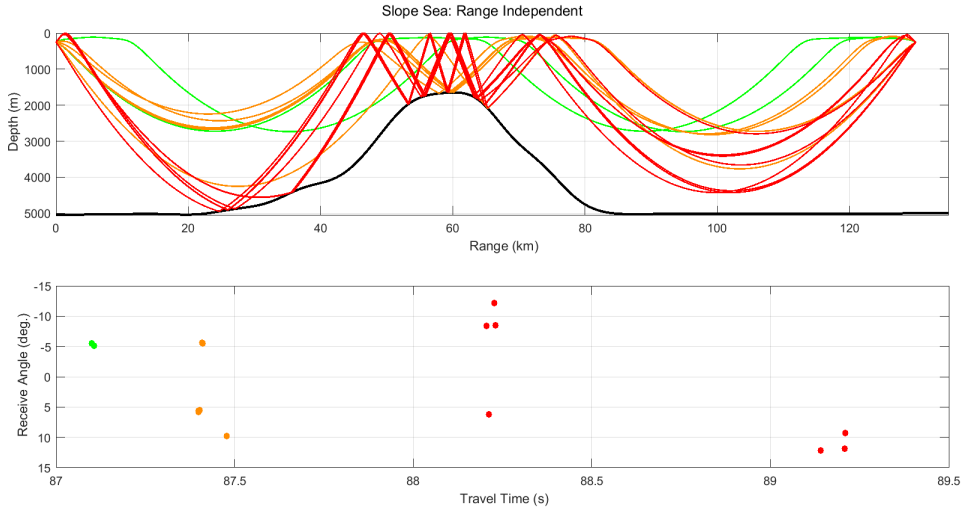

Eigenray paths (top) and their respective source receive angles (bottom) are categorized by their number of boundary interactions (BIs). Green eigenrays indicate one or no BIs, yellow eigenrays indicate two BIs, and red eigenrays indicate three or more BIs.

Figure 28. Slope Range Independent Rays (SD = 250m, R = 130km)

2. Range Dependent Acoustic Propagation

In order to estimate the range-dependent acoustic path fluctuations which are provoked by high frequency IW propagation, a simulated IW field was integrated into the source-receiver tactical scenario in the Sargasso and Slope Seas. Although oceanographic data collected by EMV-1B could be applied to simulate acoustic propagation by investigating the temporal and spatial changes of the SSP at the discrete mooring location, this methodology would fail to account for the range-dependent acoustic variability induced by an IW field which may alter the propagation path of an eigenray as it travels between the source and receiver. This simulated IW field, originating from GM variance approximations which align with measured isotherm spectral energy, produces range-dependent sound speed fluctuations (δc) which will modify the range-independent ray paths portrayed in Figures 25–28. Figures 29 and 30 display the range-dependent sound speed fluctuations facilitated by simulated IW activity in the Sargasso and Slope Sea alongside the SSP used for each water mass. As expressed in Equation 1.3, depth regions with strong sound speed gradients are associated with substantial sound speed fluctuations (Figures 29 and 30). The reader should note that Figures 29 and 30 possess different sound speed fluctuation contour scales. With this discontinuity in mind, sound speed fluctuations feature higher magnitudes in the Slope Sea than in the Sargasso Sea (Figures 29 and 30), which aligns with EMV-1B potential density anomaly standard deviations (Figure 6), observed high pass isotherm oscillation trends (Figures 13 and 14), and IW spectral variance magnitudes (Table 4).

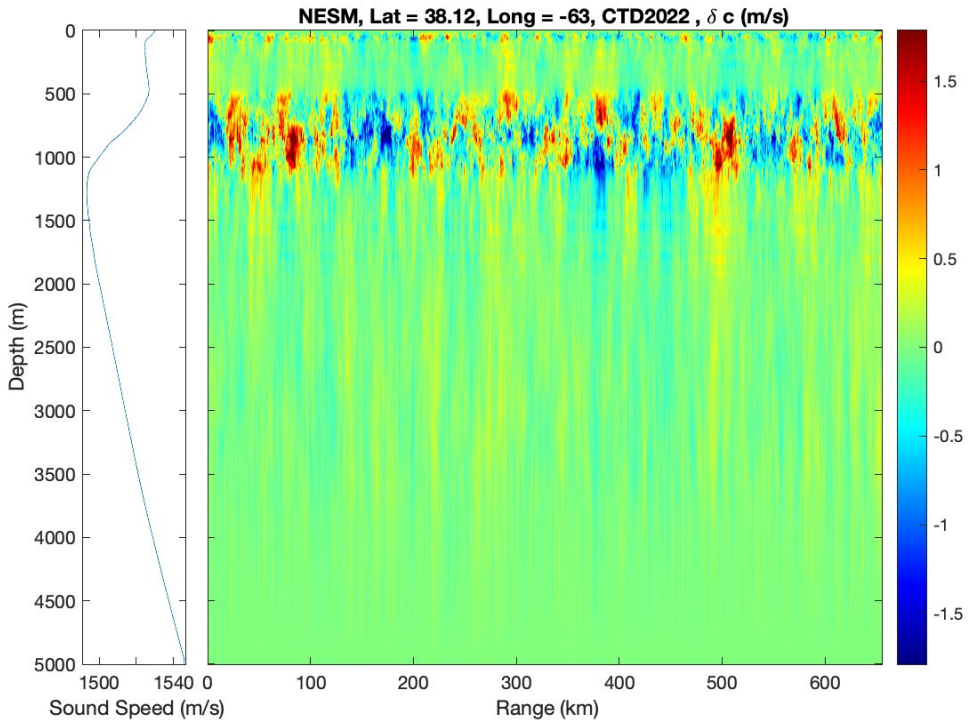

Figure 29. Sargasso Sea Simulated Sound Speed Variability

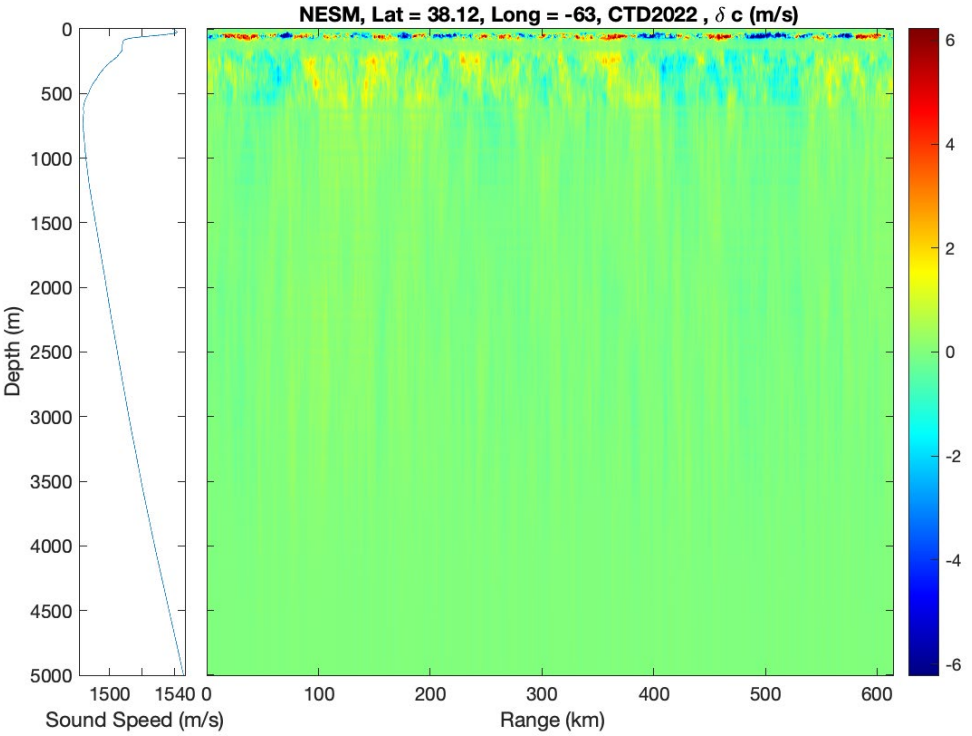

Figure 30. Slope Sea Simulated Sound Speed Variability

Range independent eigenrays (annotated in light green and identical to those previously discussed in Figures 25–28) and range dependent eigenrays (annotated in black and modified by the sound speed fluctuations represented in Figures 29 and 30) are compared in this section to visualize the impact of an IW field on acoustic path availability. All range dependent eigenray plots experience a gain, modification, or loss of range independent acoustic paths due to the presence of a simulated IW field. Range dependent acoustic paths and eigenray receive angles for the Sargasso Sea with the source and receiver at a 250-meter depth and separated by a range of 61 kilometers is shown in Figure 31. The eigenrays, upon realization of the IW field, exponentially increase (28 to 179) between the source and receiver, which is a common phenomenon in most of the range dependent eigenray plots covered in this chapter and a defining characteristic of chaotic acoustic ray behavior (Figure 31). The Sargasso Sea 61-kilometer plot features an increase in both seafloor BI rays and subsurface ducted rays (Figure 31). As range increases to 130 kilometers, the Sargasso Sea acoustic paths demonstrate a majority of eigenrays refracting within the Sargasso Sea subsurface duct before diverging into an array of CZ paths on the opposite side of A2 (Figure 32). This eigenray scattering effect is a product of the IW field (Figure 32).

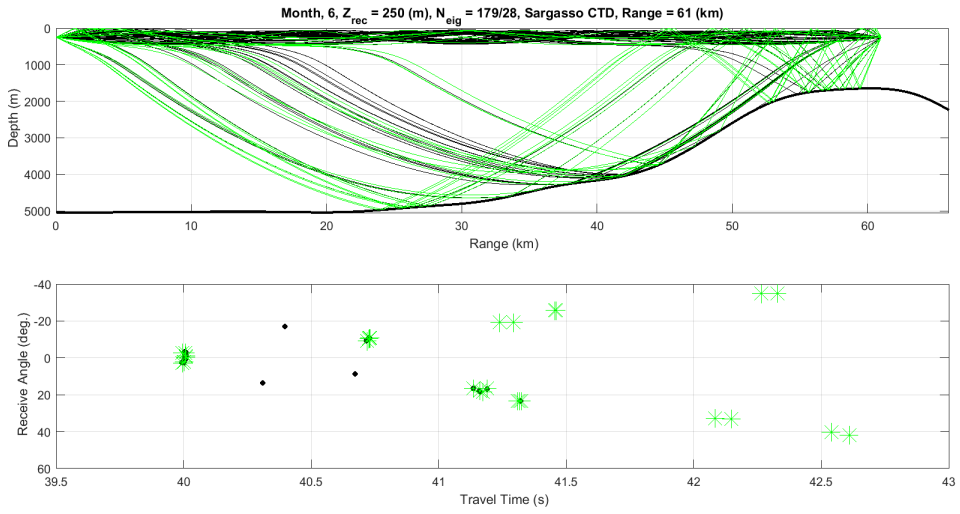

Eigenray paths (top) and their respective source receive angles (bottom) include range independent (shaded light green) and range dependent (shaded black) rays.

Figure 31. Sargasso Range Dependent Rays (SD = 250m, R = 61km)

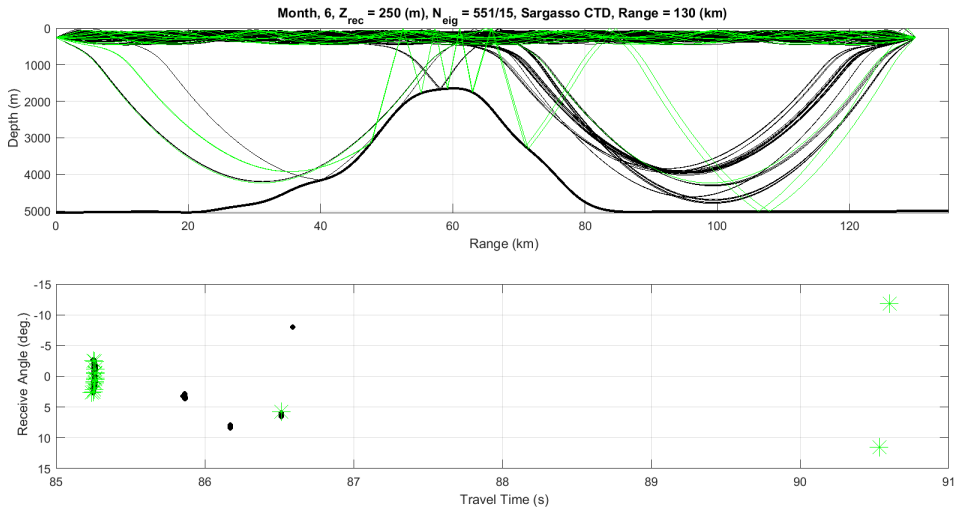

Eigenray paths (top) and their respective source receive angles (bottom) include range independent (shaded light green) and range dependent (shaded black) rays.

Figure 32. Sargasso Range Dependent Rays (SD = 250m, R = 130km)

The range dependent acoustic paths and eigenray receive angles for the Slope Sea with the source and receiver at a 250-meter depth and a range of 61 kilometers is shown in Figure 33. IWs appear to create more Slope Sea CZ eigenrays in the range dependent paths compared to the range independent paths (Figure 33). The range dependent acoustic paths in the Slope Sea for a range of 130 kilometers is illustrated in Figure 34. Many range-dependent eigenrays behave similarly to CZ rays but appear to be bundled together and have a BI with the summit of A2 before continuing towards the receiver, which is an interesting multi-path ray pattern (Figure 34).

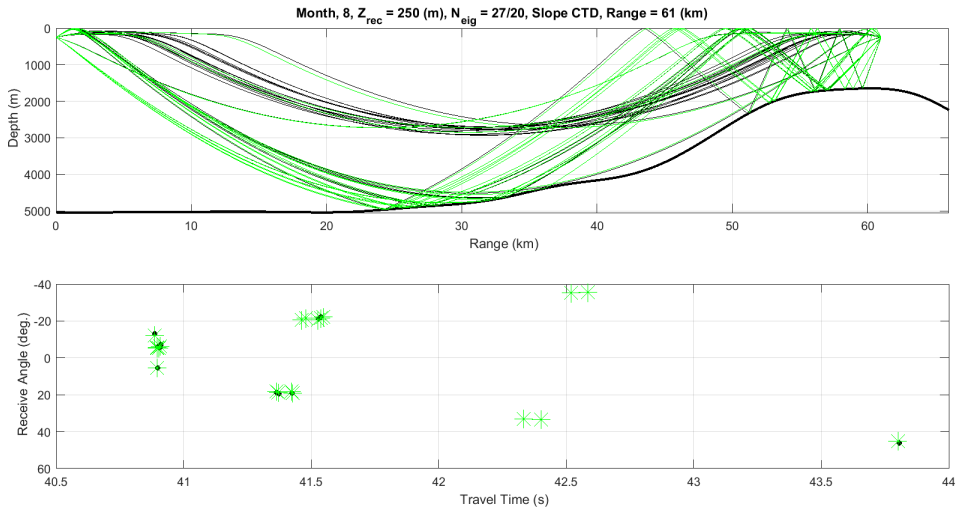

Eigenray paths (top) and their respective source receive angles (bottom) include range independent (shaded light green) and range dependent (shaded black) rays.

Figure 33. Slope Range Dependent Rays (SD = 250m, R = 61km)

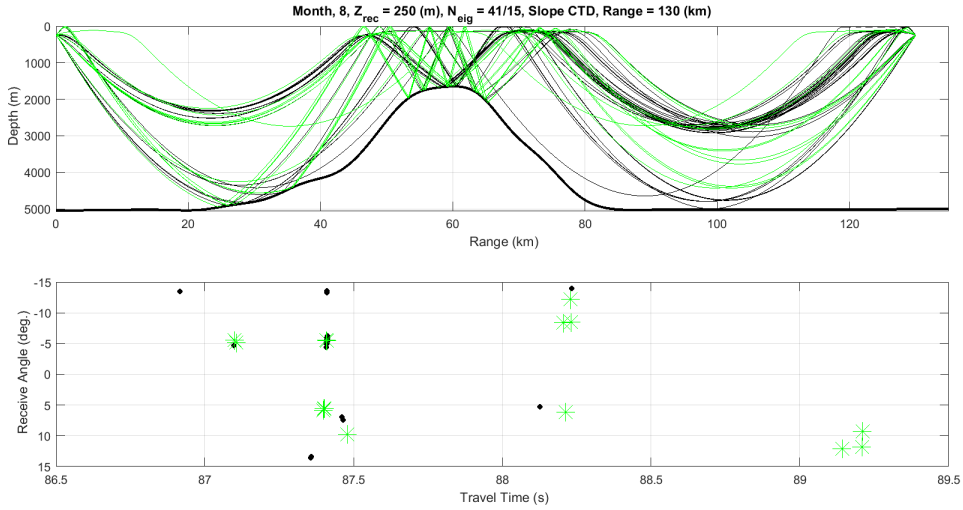

Eigenray paths (top) and their respective source receive angles (bottom) include range independent (shaded light green) and range dependent (shaded black) rays.

Figure 34. Slope Range Dependent Rays (SD = 250m, R = 130km)

3. IW Time Evolution of Sargasso Sea Ray Paths

Figures 35–37 capture the twenty-minute time evolution of range dependent acoustic ray paths within a simulated IW field in the Sargasso Sea for a 700-meter source

depth (which is deeper than the 250-meter case discussed previously) and 250-meter receiver depth at a range of 130 kilometers. Range dependent rays are outlined in black while range independent rays are shown in light green. The range independent paths (green) observed in Figures 35–37 are consistent with the most reliable range independent eigenrays featured earlier in Figure 26 despite the source depth inconsistency. Figures 35–37 illustrate volatile chaotic ray behavior as eigenrays interact with the simulated IW field at tactically significant timescales (10-minute intervals). The initial timestep (t = 0 min) features refracted eigenrays within the subsurface duct which evolve into complex BI multi-path rays after passing over the A2 summit (Figure 35). IW-modified eigenrays at the initial timestep also indicate more CZ path availability, and curiously, some of this CZ energy is scattered into the subsurface duct by the IW field near the A2 summit (Figure 35). After ten minutes of simulated IW field evolution, the amount of range dependent eigenrays is more than double the amount present in the initial timestep (Figure 36). The IW field at ten minutes appears to preserve a complete subsurface ducted acoustic path without any scattering at the 130-kilometer range and maintain an assortment of available ducted CZ acoustic paths (Figure 36). The twenty-minute timestep indicates a loss of the complete subsurface ducted acoustic path observed at the 10-minute timestep (Figure 36) and features acoustic scattering from CZ acoustic paths into the subsurface duct over A2 (Figure 37).

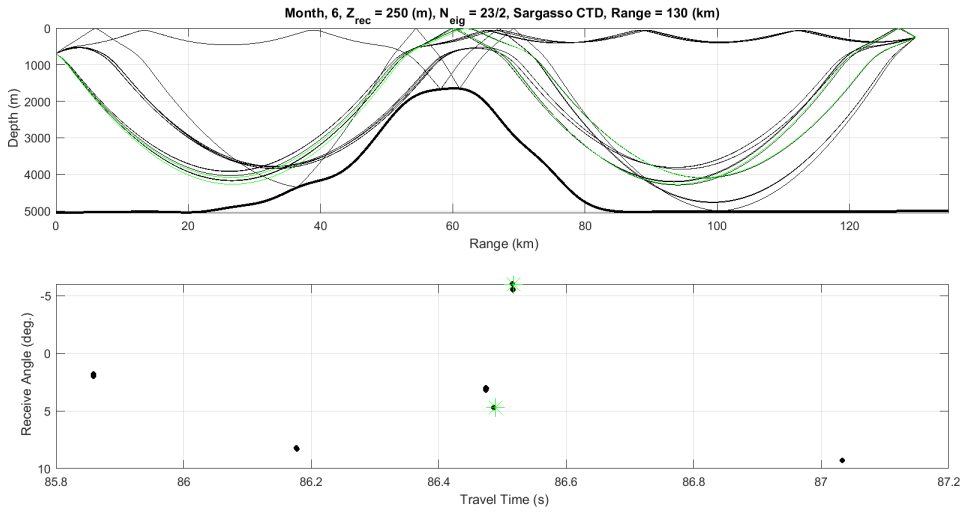

Eigenray paths (top) and their respective source receive angles (bottom) include range independent (shaded light green) and range dependent (shaded black) rays.

Figure 35. Sargasso Range Dependent Rays (SD = 700m, t = 0min)

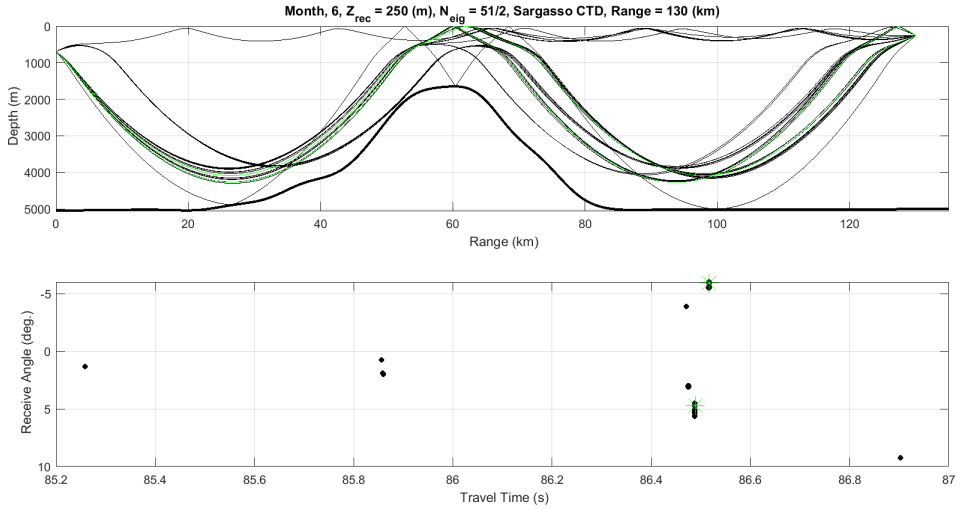

Eigenray paths (top) and their respective source receive angles (bottom) include range independent (shaded light green) and range dependent (shaded black) rays.

Figure 36. Sargasso Range Dependent Rays (SD = 700m, t = 10min)

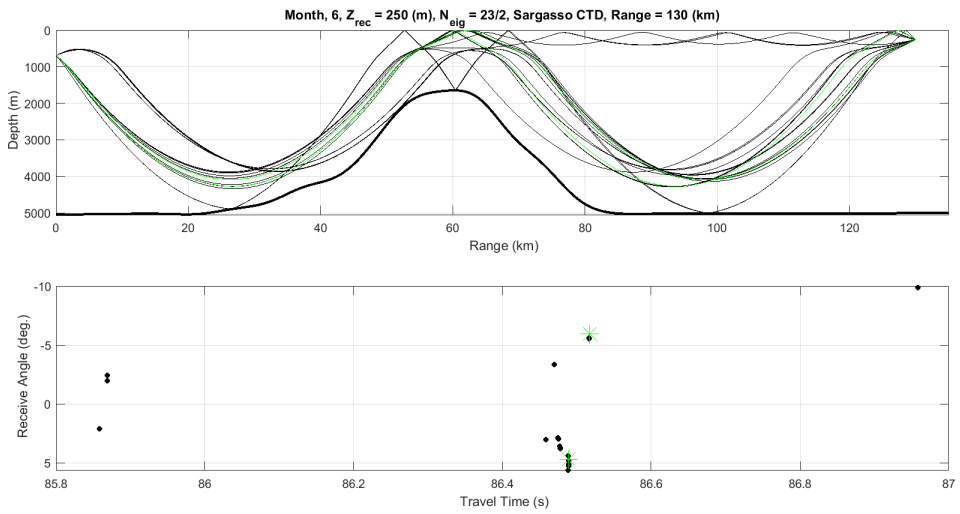

Eigenray paths (top) and their respective source receive angles (bottom) include range independent (shaded light green) and range dependent (shaded black) rays.

Figure 37. Sargasso Range Dependent Rays (SD = 700m, t = 20min)

Figures 35–37 indicate that CZ and subsurface ducted rays are the most reliable long-range acoustic paths in this range dependent scenario in the Sargasso Sea. CZ propagation appears consistently for a source depth of 700 meters, but subsurface ducted ray paths appear more variable as time progresses. Therefore, CZ paths and receive angles in the Sargasso Sea provide the most likely means of detecting an acoustic signal in this simulation (Figures 35–37). These reliable paths and receive angles chaotically evolve over time, and this unpredictability could adversely impact SONAR system performance if unexpected.

4. IW Time Evolution of Slope Sea Ray Paths

Figures 38–40 capture the twenty-minute time progression of range dependent acoustic ray paths within a simulated IW field in the Slope Sea for a 250-meter source and receiver at a range of 130 kilometers. Range dependent rays are still outlined in black, and range independent rays are shown in light green. In a similar manner to the Sargasso Sea IW time evolution figures, the Slope Sea range independent paths (green) observed in Figures 38–40 are consistent with the low BI range independent eigenrays displayed in Figure 28. The range dependent eigenrays (black) also indicate that chaotic ray activity

occurs at all Slope Sea timesteps (Figures 38–40). The Slope Sea initial timestep (t = 0) features CZ eigenrays reflecting off the A2 summit, which is a phenomenon also observed in the Sargasso Sea (Figures 35–37) and appear to be the most reliable acoustic path in this timestep (Figure 38). The ten-minute and twenty-minute timestep do not appear to possess any significant acoustic path alterations, but certainly indicate that the IW field is affecting eigenray paths and receive angle (Figures 39 and 40).

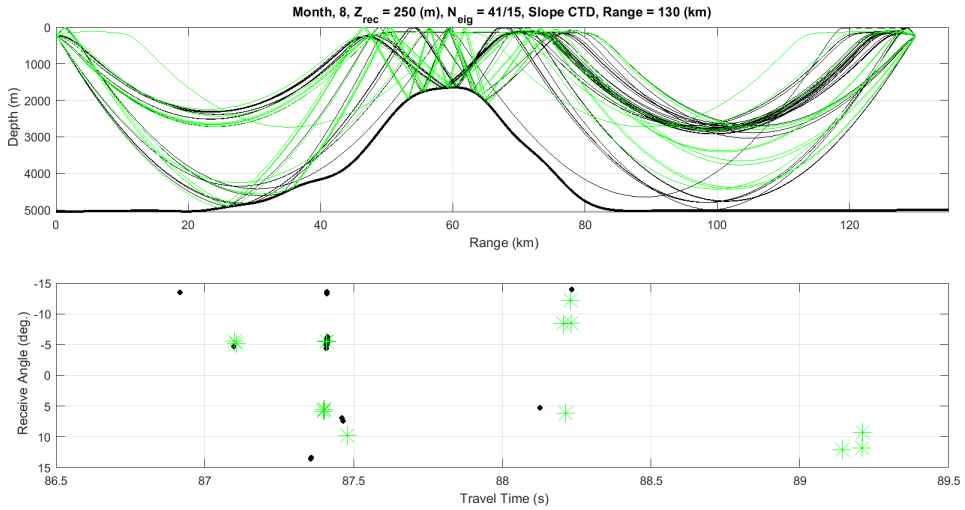

Eigenray paths (top) and their respective source receive angles (bottom) include range independent (shaded light green) and range dependent (shaded black) rays.

Figure 38. Slope Range Dependent Rays (SD = 250m, t = 0min)

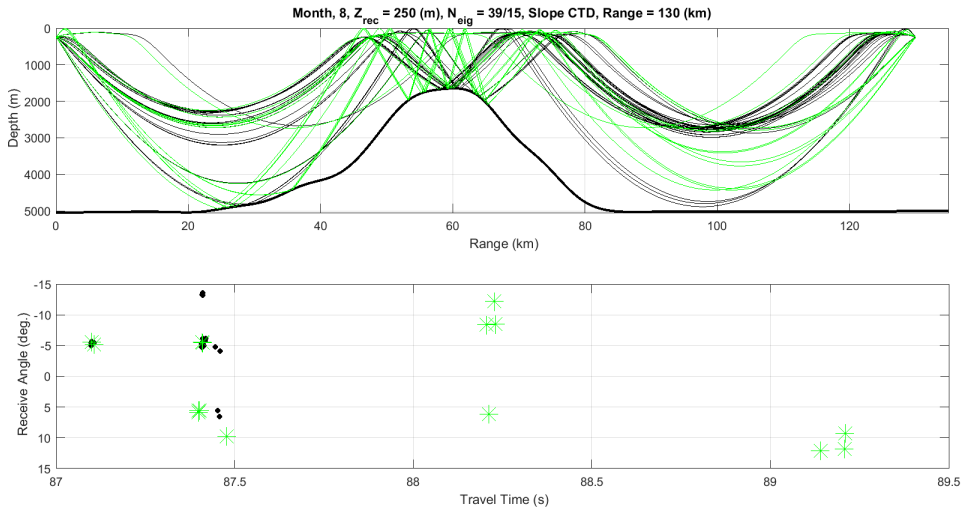

Eigenray paths (top) and their respective source receive angles (bottom) include range independent (shaded light green) and range dependent (shaded black) rays.

Figure 39. Slope Range Dependent Rays (SD = 250m, t = 10min)

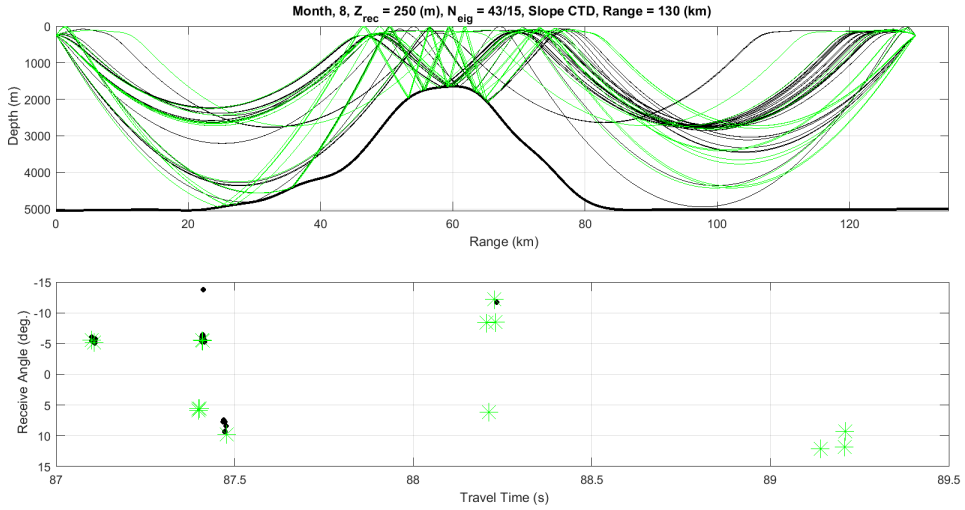

Eigenray paths (top) and their respective source receive angles (bottom) include range independent (shaded light green) and range dependent (shaded black) rays.

Figure 40. Slope Range Dependent Rays (SD = 250m, t = 20min)

Figures 38–40 indicate that CZ and bottom bounce rays are the most reliable long-range acoustic paths in this range dependent scenario in the Slope Sea. Both CZ and bottom bounce propagation appears consistent for a source depth of 250 meters, but reliable paths

and receive angles in the Slope Sea chaotically evolve in time (Figures 38–40) in a similar manner to the Sargasso Sea range dependent simulations (Figures 35–37).

V. CONCLUSIONS

This thesis analyzed in-situ oceanographic data to identify eddies, ITs, and random IWs in the Sargasso and Slope Sea above a caldera in the NESC and quantified how their presence can influence the surrounding acoustic field, modify waveguides, and disrupt anticipated acoustic paths. Interpolated isotherms, which are assumed to be an effective stand-in for isopycnal surfaces, suggest the dominance of a semidiurnal IT and an energetic IW field in the water column above the caldera (Figures 13 and 14). Typical vertical isotherm displacements reach 70 meters in the Sargasso Sea and 150 meters in the Slope Sea (Figures 13 and 14). Isotherm vertical displacements on IW temporal scales do not appear to possess varying energy during low frequency isotherm depression and elevation events, which suggests that the IW field over the caldera is not discernably influenced by eddies or Gulf Stream filaments (Figures 11 and 12). A more detailed analysis is needed to study the relationship between vertical isotherm displacements and oceanographic processes at larger temporal scales. Buoyancy-averaged isotherm displacement spectra in the Sargasso and Slope Sea possess a powerful semidiurnal IT and IT harmonics, which implies that a portion of the IW field (energy at semidiurnal and harmonic frequencies) over the caldera is locally generated. Prominently larger IW variances in deeper isotherm groups (Table 4) and higher measured to theoretical GM variance ratios (Table 5) support the suspicion of a locally generated IW field and suggest that the water column above the caldera is subject to nonlinear IW behavior. The origin of random, high frequency IWs present in isotherm spectra is difficult to determine. The duct width (Figure 21), length (Figure 21), and maximum mode number (Figure 22) of the Sargasso Sea subsurface duct suggests that IW activity, at the dominant frequencies found in the upper ocean Sargasso Sea spectra (Figure 15), are subject to significant variability. Range-dependent acoustic paths in the Sargasso and Slope Sea demonstrated ray chaos, or the nonlinear creation and destruction of available acoustic paths, as eigenrays propagated through a simulated IW field in 10-minute intervals (Figures 35–40).

Comprehension of the presence and generating conditions of ITs and IWs in the NESC, which can complicate the transmission of acoustic signals and alter the ambient

noise field, is an essential step towards acquiring a tactical advantage in this complex environment. Acoustic path availability is the beginning of any tactical analysis of the ocean acoustic field. Once available paths are identified, the impacts of IW fields and their associated sound speed fluctuations can be used to compute statistics of the acoustic field. Such statistics include signal coherence, which is important for SONAR array performance, and scintillation, which is essential for target detection during signal "twinkle" and conceptualizing the time between signal twinkles and fadeouts. These factors can drastically impact a SONAR operator's ability to detect, classify, and track a target. Further, a time and range dependent statistical analysis of these signal properties and their impacts on signal excess would be an immense benefit to those wishing to further understand the acoustic impacts of IWs. A two-dimensional ray model near a complex topographic feature only partially represents the true behavior of propagating sound in a four-dimensional environment, and further NESC acoustic research will hopefully illuminate this region's specific acoustic arrival patterns.

This thesis did not investigate vertical shear or current speed over the caldera, which was measured by acoustic doppler current profilers while the EMV-1B mooring was deployed. The Gulf Stream frontal passage measured by EMV-1B likely introduced considerable kinetic energy and vertical shear into the water column above the NESC, and an anomaly of typical Froude or Richardson number magnitudes could have occurred. An evaluation of current speeds, hydraulic control, and their relationship with IW energy in time could reveal fascinating results. With one mooring alone, it is challenging to determine whether the measured IW field is generated by the caldera, other topographic features in the NESC, or from topography a great distance away. An array of vertical moorings with oceanographic instruments near the NESC, including a mooring along the slope of a seamount, would aid in further classifying the characteristic IW field present in the water column above. An array of vertical moorings would also grant an opportunity to approximate IW speed and directionality, which is challenging to determine with a single vertical mooring. Further research could discuss the presence or formation conditions of tidal bores near A2 and whether tidal beams are likely to disturb the upper ocean pycnocline in the Sargasso and Slope Sea and generate a soliton. The Task Force Ocean field programs

for 2023 and 2024 will be probing these very questions to make the important linkages between acoustics (both signal and noise) and physical oceanographic and geological processes.

THIS PAGE INTENTIONALLY LEFT BLANK

LIST OF REFERENCES

Akylas, T., Grimshaw, R., Clarke, S., & Tabaei, A. (2007). Reflecting tidal wave beams and local generation of solitary waves in the ocean thermocline. *Journal of Fluid Mechanics*, *593*, 297–313.

Baxter, L. & Orr, M. H. (1982). Fluctuations in sound transmission through internal waves associated with the thermocline: A computer model for acoustic transmission through sound velocity fields calculated from thermistor chain, CTD, XBT, and acoustic backscattering. *The Journal of the Acoustical Society of America*, *71*(1), 61–66.

Beron-Vera, F.J., Brown, M.G., Colosi, J.A., Tomsovic, S., Virovylansky, A.L., Wolfson, M.A., and Zaslavsky, G.M. (2003). Ray dynamics in a long-range acoustic propagation experiment. J. Acoust. Soc. Am., *114*, 1226–1241.

Brickman, D., & Loder, J. W. (1993). Energetics of the internal tide on northern Georges Bank. Journal of Physical Oceanography, *23*(3), 409–424.

Brown, M.G., Colosi, J.A., Virovlyansky, A.L., Zaslavsky, G. M., Tomsovic, S., and Wolfson, M. A. 2003. Ray dynamics in ocean acoustics. J. Acoust. Soc. Am., *113*, 2533–2547.

Chaytor, J. (2022). *Atlantis II seamount survey area. Overview of the NESM pilot and new results associated with surface and subsurface ducting* [Presentation].

Colosi, J.. (2022). *NESC TFO study area. Overview of the NESM pilot and new results associated with surface and subsurface ducting* [Presentation].

Colosi, J. (2016). *Sound propagation through the stochastic ocean*. Cambridge University Press.

Colosi, J., Duda, T. F., Lin, Y.-T., Lynch, J. F., Newhall, A. E., & Cornuelle, B. D. (2012). Observations of sound-speed fluctuations on the New Jersey continental shelf in the summer of 2006, *J. Acoust. Soc. Am*., *131*, 1733–1748.

Colosi, J., Van Uffelen, L. J., Cornuelle, B. D., Dzieciuch, M. A., Worcester, P. F., Dushaw, B. D., & Ramp, S. R. (2013). Observations of sound-speed fluctuations in the western Philippine Sea in the spring of 2009, *J. Acoust. Soc. Am*., *134*, 3185–3200.

Duncan, A.J., Parnum, I.M., & MacLeod, R. (2018). The effect of internal waves on sound propagation parallel to the internal wave crests. Australian Acoustical Society 2018 Proceedings of Acoustics Conference, 1–10. https://acoustics.asn.au/conference_proceedings/AAS2018/papers/p57.pdf

Etter, P. (2014). *Underwater acoustic modeling and simulation* (3rd ed.). CRC Press.

Ezer, T. (1994). On the Interaction between the Gulf Stream and the New England Seamount Chain, *Journal of Physical Oceanography*, *24*(1), 191–204.

Fofonoff, P. & Millard, R. (1983). *Algorithms for computation of fundamental properties of seawater*. UNESCO Technical Paper in Marine Science, 44.

Gao, Hu, P., Xu, F., Li, Z., & Qin, J. (2023). Effects of internal waves on acoustic temporal coherence in the South China Sea. *Journal of Marine Science and Engineering*, *11*(2).

Gerkema, T. & Zimmerman, J. T. *An introduction to internal waves*. Lecture notes, Royal NOIZ, Texel, The Netherlands, 2008, 147–164.

He, Xie, H., Zhang, Z., & Liu, S. (2022). Numerical investigation of internal solitary wave forces on a moving submarine. *Journal of Marine Science and Engineering*, *10*(8), 1020–1025. https://doi.org/10.3390/jmse10081020

Kemp, J. & Ryder, J. (2022). *EMV-1B Mooring as Deployed. Mooring Operations and Engineering. Woods Hole Oceanographic Institution.* Overview of the NESM pilot and new results associated with surface and subsurface ducting [Presentation].

Levine, M. D., and Richman, J. G. (1989). Extracting the internal tide from data: Methods and observations from the Mixed Layer Dynamics Experiment, *J. Geophys. Res*., *94*(C6), 8125– 8134.

Munk, W. (1981). " Internal waves and small scale processes" in *The Evolution of Physical Oceanography*, edited by B. Warren and C. Wunsch (MIT, Cambridge, MA), pp. 264–291.

Nam, S., & Chen, X. (2022). Oceanic internal waves and internal tides in the East Asian marginal seas. *Journal of Marine Science and Engineering*, *10*(5), 573. MDPI AG. Retrieved from http://dx.doi.org/10.3390/jmse10050573

National Park Service. (2023). Calderas [Fact sheet]. https://www.nps.gov/articles/000/calderas.htm

Palmer, M. R., Inall, M. E., & Sharples, J. (2013). Physical oceanography of Jones Bank: A mixing hotspot in the Celtic Sea. *Progress in Oceanography*, *117*, 9–24.

Parnum, I.M., MacLeod, R., Duncan, A.J., & Gavrilov, A.N. (2017). The effect of internal waves on underwater sound propagation. *Australian Acoustical Society 2017 Proceedings of Acoustics Conference*, 1–9. https://acoustics.asn.au/conference_proceedings/AAS2017/papers/p76.pdf

Shank, T. M. (2010). SPOTLIGHT 4 | New England and corner rise seamounts. *Oceanography* (Washington, D.C.), *23*(1), 104–105. https://doi.org/10.5670/oceanog.2010.76

Stashchuk, N. & Vlasenko, V. (2021). Internal wave dynamics over isolated seamount and its influence on coral larvae dispersion. *Frontiers in Marine Science*, *8*.

Stashchuk, N., Vlasenko, V., and Howell, K. L. (2018). Modeling tidally induced larval dispersal over Anton Dohrn Seamount. Ocean Dyn. *68*, 1515–1526.

Vlasenko, V., Stashchuk, N., & Nimmo-Smith, W. A. M. (2018). Three-dimensional dynamics of baroclinic tides over a seamount. *Journal of Geophysical Research. Oceans*, *123*(2), 1263–1285.

Vlasenko, V., Stashchuk, N., Palmer, M. R., & Inall, M. E. (2013). Generation of baroclinic tides over an isolated underwater bank. *Journal of Geophysical Research. Oceans*, *118*(9), 4395–4408.

Wang, T., Huang, X., Zhao, W., Zheng, S., Yang, Y., & Tian, J. (2022). Internal solitary wave activities near the indonesian submarine wreck site inferred from satellite images. *Journal of Marine Science and Engineering*, *10*(2), 197.

Yesson, C., Clark, M. R., Taylor, M. L., & Rogers, A. D. (2011). The global distribution of seamounts based on 30 arc seconds bathymetry data. Deep-Sea Research. *Part I, Oceanographic Research Papers*, *58*(4), 442–453. https://doi.org/10.1016/j.dsr.2011.02.004

Wang, J., Ingram, R.G., & Mysak, L.A. (1991). Variability of internal tides in the laurentian channel, *J. Geophys. Res*. *96*(16), 859–16875.

Wessel, P., Sandwell, D. T., & Kim, S.S. (2010). The global seamount census. *Oceanography*, *23*(1), 24–33. http://www.jstor.org/stable/24861056

Zhou, J.X., Zhang, X.Z., & Rogers, P. H. (1991). Resonant interaction of sound wave with internal solitons in the coastal zone. *The Journal of the Acoustical Society of America*, *90*(4), 2042–2054. https://doi.org/10.1121/1.401632

THIS PAGE INTENTIONALLY LEFT BLANK

INITIAL DISTRIBUTION LIST

1. Defense Technical Information Center
   Ft. Belvoir, Virginia

2. Dudley Knox Library
   Naval Postgraduate School
   Monterey, California